# Supplementary Materials for

## Architecture of the MKK6-p38α complex defines the basis of MAPK specificity and activation

Pauline Juyoux *et al*.

Corresponding authors: Francesco Luigi Gervasio, francesco.gervasio@unige.ch; Erika Pellegrini, epellegr@embl.fr;
Matthew W. Bowler, mbowler@embl.fr

*Science* **381**, 1217 (2023)
DOI: 10.1126/science.add7859

**The PDF file includes:**

Materials and Methods
Supplementary Text
Figs. S1 to S16
Tables S1 to S4, S6 to S10
References

**Other Supplementary Material for this manuscript includes the following:**

MDAR Reproducibility Checklist
Table S5
Movies S1 to S16

## Materials and Methods

### Plasmids

Plasmids were ordered from GenScript (gene synthesis, cloning and mutagenesis). For recombinant protein expression, human p38α sequences (WT, T180V, Y182F, and K53A mutants) were fused to a His6 tag with a 3C protease cleavage site and cloned into a pET-28b vector; MKK6$^{DD}$GRA sequence (constitutively active S207D T211D mutant of human MKK6 with GRA24 KIM) was fused to a twin StrepII tag with a 3C cleavage site and cloned into a pFastBac1 vector. For cellular reporter assays, p38α and MKK6$^{DD}$ mutant sequences were cloned into pcDNA3.1 plasmids. The lambda Phosphatase plasmid was obtained from Addgene (a gift from John Chodera & Nicholas Levinson & Markus Seeliger; Addgene plasmid #79748; http://n2t.net/addgene:79748 ; RRID:Addgene_79748) (*67*).

### Protein expression and purification

Constructs of p38α were co-transformed with the lambda phosphatase plasmid into Rosetta™(DE3)pLysS *E. coli* competent cells (Novagen) with appropriate antibiotics. Cells were grown in LB at 37°C until the OD600 = 0.6-0.8, induced with 0.5 mM IPTG, incubated at 16°C overnight, and harvested by centrifugation.

The MKK6$^{DD}$GRA constructs were transformed into DH10 EMBacY *E. coli* cells to produce recombinant baculoviruses subsequently used for protein expression in *Sf21* insect cells (*68*). Cells were harvested 48h after proliferation arrest by centrifugation.

Cell pellets were resuspended in lysis buffer (50 mM HEPES pH 7.5, 200 mM NaCl, 10 mM $MgCl_2$, 5% glycerol, 0.5 mM TCEP, with a Pierce protease inhibitor EDTA-free tablet (Thermo Scientific) and a trace of DNaseI (Sigma)). Cells were lysed by sonication on ice and the lysate cleared by centrifugation.

For p38α, supernatant was loaded onto a pre-packed 5 ml HisTrap column (GE Healthcare), equilibrated according to the supplier's protocols with wash buffer (50 mM HEPES pH 7.5, 200 mM NaCl, 10 mM $MgCl_2$, 5 % glycerol, 0.5 mM TCEP) with 1% elution buffer (wash buffer with 500 mM Imidazole). Tagged-protein was eluted with elution buffer and p38α-containing fractions were pooled, incubated with 3C-protease and dialysed against wash buffer at 4°C overnight. The sample was run through the HisTrap column again to remove uncleaved protein and flow-through fractions were collected.

For MKK6$^{DD}$GRA, supernatant was loaded onto a pre-packed 5 ml StrepTactin XT column (IBA), equilibrated according to the supplier's protocols with wash buffer. Tagged-protein was eluted with elution buffer (wash buffer with 50 mM Biotin), and MKK6-containing fractions were pooled, incubated with 3C-protease and dialysed against wash buffer at 4 °C overnight. The sample was run through the StrepTactin XT column again to remove uncleaved protein, HisTrap column to remove the protease, and flow-through fractions were collected.

Pure proteins were concentrated using 10 kDa Amicon Ultra membrane concentrators (Millipore), flash-frozen in liquid nitrogen and stored at -80℃.

In order to prepare the hetero-kinase complex, MKK6$^{DD}$GRA and p38α aliquots were thawed, mixed in 1:1 mass ratio and incubated on ice for 1h. The sample was then concentrated to 10 mg/ml with a 10 kDa Amicon Ultra membrane concentrators (Millipore) and loaded onto a Superdex S200 increase 10/300 GL size-exclusion column (GE Healthcare) equilibrated in wash buffer (with a reduced glycerol concentration of 2% when for cryo-EM studies). Purest peak fractions were pooled, flash-frozen in liquid nitrogen and stored at -80°C before being used for structural studies or biochemical assays.

SAXS

MKK6$^{DD}$GRA-p38α complexes purified by gel filtration were complemented with either 10 mM ADP, 10 mM $NH_4F$ and 1 mM $AlCl_3$ or 10 mM AMP-PCP and incubated on ice for 30 minutes before proceeding.

Small Angle X-ray Scattering data were collected at the bioSAXS beamline B21 at the Diamond Light Source (DLS), UK (proposal SM23091-1). Scattering curves were measured from solutions of the different MKK6$^{DD}$GRA-p38α samples in SAXS buffer (50 mM HEPES pH 7.5, 200 mM NaCl, 10 mM $MgCl_2$, 5 % glycerol, 0.5 mM TCEP). Buffer subtractions and all other subsequent analyses were performed with the program Scatter IV (*69*) and SAXS profile computation used FoXS (*70*) (Table S10).

Cryo-EM specimen preparation and data collection

Purified MKK6$^{DD}$GRA-p38α$^{T180V}$ was complemented with 250 µM AMP-CP, 250 µM $NH_4F$ and 25 µM $AlCl_3$, and incubated on ice for 30 minutes before proceeding. UltraAufoil 1.2/1.3 grids were glow-discharged for 30 seconds at 25 mA (PELCO easy glow). During the vitrification procedure on a Vitrobot Mark IV (FEI), 4 µl of sample at 6 µM concentration was applied to the grid. The blotting force was set to 0 for a total time of 3.5 seconds. Grids were then clipped and screened on a FEI Talos Glacios electron microscope (EMBL Grenoble) operating at 200 kV. Selected grids were then sent for data collection on a FEI Titan Krios (EMBL Heidelberg) operating at 300 kV (*71*). Micrographs were automatically collected using SerialEM (*72*) from a K2 Quantum detector (Gatan) and a GIF Quantum energy filter (Gatan), at a nominal magnification of 215,000 (corresponding to 0.638 Å/pixel at the specimen level). Three different data collections with a total of 28,633 movies of 40 frames were collected in electron counting mode with a defocus range of -1.5 to -3 µm, 0.1 µm step, with a total exposure of 62.77 $e^-/Å^2$.

Cryo-EM processing

Each dataset was treated independently following a similar workflow and the best particles corresponding to the hetero-kinase sample were finally combined and further processed.

Movies were imported into cryoSPARC *(65)*. All movie frames were aligned and motion-corrected with Patch Motion correction and CTF estimated with Patch CTF. Data were manually curated to eliminate micrographs with large motions, poor resolution, and high ice thickness. The resulting micrographs showed a low signal/noise ratio, but classical picking with a blob picker failed to identify particles. We successfully picked a large number of particles by using a combination of Topaz particle picker *(32)* and template picker. Particles were extracted with a box size of 300 x 300 pixels and 2D classification was used to eliminate junk and the noisiest particles. We then applied *ab-initio* and heterogeneous refinement, requesting 3-6 models and particles corresponding to the hetero kinase model were selected for further 2D classification. Between 2-3 rounds of 2D classification were necessary to select good particles, showing secondary structural features and low background noise. Non-uniform refinement was then used to obtain a ~5 Å resolution map. An exemplary workflow is shown in Figure S3A for dataset 2.

To improve resolution, we then combined selected particles from each dataset (86,510 particles in total), and we applied 2D classification, *ab-initio,* heterogeneous and non-uniform refinement to select between face-to-face conformations where the A-loop was visible or dynamic allowing us to obtain a final map at 4.00 Å resolution, corresponding to 35,123 particles (Fig. S3B). Maps were sharpened in cryoSPARC and using locscale (*73*).

The initial model was built from the combination of different structures: the crystal structure of p38α WT presenting an ordered activation loop (PDB-5ETC), the crystal structure of p38α bound to GRA24 KIM peptide (PDB-5ETA) *(31)*, and a homology model of MKK6$^{DD}$ based on the crystal structure of the active MKK7$^{DD}$ structure (PDB-6YG1) *(16)* obtained with SWISS-MODEL (*74*). The model of each kinase was individually docked into the map as a rigid body using the phenix.place.model and then refined with one round of morphing and real space refinement using Phenix.refine (*75*) and corrected in COOT (*76*). To validate the rebuilt model, we relied on cross-correlation calculations between the experimental maps and those predicted from the MD simulations to select the model that best recapitulates the available data. We considered a set of 87 structures including the rebuilt model, AF2 predictions, complex structures including the linker and p38α activation loop modelled using the *automodel* functionality of MODELLER, and 79 clusters extracted from one relevant MD simulation showing p38α Y182 close to MKK6 ATP (rep4 with restraints). Given the sensitivity of cross-correlation calculations to atomic B-factors, we re-assigned temperature factors for each structure using Phenix by running one round of refinement with default parameters. This step allowed us to compare the cross-correlation scores assigned to all the models in the dataset. Cross-correlation scores were then computed considering the entire complex and a selection of key structural features, i.e., hydrophobic patch, KIM, p38α activation loop, and the MKK6 region close to the resolved linker (details in Table S3). By selecting a specific region of the structure, cross-correlation was computed in the area surrounding the selection only. Considering the entire complex, the rebuilt model was assigned the highest cross-correlation score. However, one of the predicted models was assigned to a higher score than the rebuilt model for the area around the hydrophobic patch, the p38α activation loop, and the MKK6 region close to the linker. Therefore, we incorporated the structural information for these features into the final model as they are in better agreement with the experimental data. Table S3 summarizes the cross-correlation scores for all structures. See Table S4 for data processing and refinement statistics. Figures were prepared in ChimeraX (*77*) and validation was performed with Phenix Comprehensive Validation.

### Crystallisation, data collection and structure determination of inactive p38α with a stable A-loop

Crystallization conditions were established by testing several commercial screens at the EMBL High Throughput Crystallisation Laboratory. Crystals of p38α$^{K53R}$ were obtained at 20°C by the sitting drop method from solutions containing 10 mg/ml p38α$^{K53R}$ in 20 mM Tris HCl pH 7.5, 150 mM NaCl, 10mM $MgCl_2$, 1mM DTT, 5% (v/v) glycerol, equilibrated against 3.5 M Na Formate pH 7.0. Crystals were transferred to a cryoprotection buffer prepared by equilibrating protein buffer solution against reservoir solution supplemented with 20% (v/v) glycerol in a sitting drop plate and harvested using a micromesh loop (MiteGen, Ithica, NY, USA), plunged into liquid nitrogen and stored at 70 K. Crystals of wild type p38α were obtained as above but equilibrated against 1.5 to 1.6 M $NH_4(SO_4)_2$, 50 mM $MgCl_2$ and 50 mM TRIS/HCl pH 8.0. Crystals were harvested directly from the mother liquor (*78*) using a micromesh loop (MiteGen, Ithica, NY, USA), plunged into liquid nitrogen and stored at 70 K. Diffraction data were collected at beamlines ID23-1 and ID23-2 at the ESRF (Grenoble, France) on an ADSC Q315 CCD detector (ID23-1) or a MAR225 CCD detector (ID23-2) to between 2.2 and 2.8 Å resolution. Crystals of p38α and p38α$^{K53R}$ contained multiple leaves of crystals and the combination of a microfocussed or micro beam in combination with automated mesh scans was essential (*79, 80*). Both p38α and p38α$^{K53R}$

crystallized in the orthorhombic space group $P2_12_12_1$ with one molecule in the asymmetric unit and similar unit cell dimensions (Table S2). Data were processed with XDS (*81*) and programs from the Collaborative Computational Project Number 4 suite (*82*). The structures were determined by molecular replacement using MolRep (*83*). For the p38α$^{K53R}$ structure, accession code 1WFC *(10)* was used as a search model with all water molecules removed. For p38α the p38α$^{K53R}$ structure was used as a search model. Refinement was carried out alternately using Phenix (*84*) and by manual rebuilding with COOT (*76*). Models were validated using Molprobity (*85*).

## AlphaFold2 predictions

AlphaFold2 multimer *(34)* was run with a local ColabFold (*86*) set-up available from https://github.com/YoshitakaMo/localcolabfold. Input sequences of MKK6 + p38α complexes were provided in csv format and run with the following option settings: `--num-recycle` 3 `--model-type` AlphaFold2-multimer-v2 `--num-models` 5. The resulting models and PAE plots were coloured using ChimeraX *(77)*.

## HDX-MS

HDX-MS experiments were performed at the UniGe Protein Platform (University of Geneva, Switzerland) following a well-established protocol with minimal modifications (*87*). Details of reaction conditions and all data are presented in Table S5. HDX reactions were done in 50 µl volumes with a final protein concentration of 5.4 µM of MKK6. Briefly, 272 picomoles of protein were pre-incubated with 815 picomoles of p38α or corresponding buffer in 5 µl final volume for 5 min at 22 °C before initiating the reaction.

Deuterium exchange reaction was initiated by adding 45 µl of $D_2O$ exchange buffer (20 mM Hepes pH 7.5 / 200 mM NaCl / 10 mM $MgCl_2$ / 500 nM TCEP / 2 mM $AlCl_3$ / 1 mM $NH_4F$ / 1 mM AMP-CP supplemented with 6 µM of p38 or equivalent buffer) to the protein mixture. Reactions were carried out at room temperature for 3 incubation times in triplicates (3 s, 30 s, 300 s) and terminated by the sequential addition of 20 µl of ice-cold quench buffer 1 (4 M Gdn-HCl / 1 M NaCl / 0.1 M $NaH_2PO_4$ pH 2.5 / 1 % Formic Acid (FA) / 200 mM TCEP in $D_2O$). Samples were immediately frozen in liquid nitrogen and stored at -80 °C for up to two weeks.

To quantify deuterium uptake into the protein, samples were thawed and injected in a UPLC system immersed on ice with 0.1 % FA as the liquid phase. The protein was digested via two immobilized pepsin columns (Thermo #23131), and peptides were collected onto a VanGuard precolumn trap (Waters). The trap was subsequently eluted, and peptides separated with a C18, 300Å, 1.7 µm particle size Fortis Bio 100 x 2.1 mm column over a gradient of 8 – 30 % buffer over 20 min at 150 µl/min (Buffer B: 0.1 % formic acid; buffer C: 100 % acetonitrile). Mass spectra were acquired on an Orbitrap Velos Pro (Thermo), for ions from 400 to 2200 m/z using an electrospray ionization source operated at 300 °C, 5 kV of ion spray voltage. Peptides were identified by data-dependent acquisition of a non-deuterated sample after MS/MS and data were analyzed by Mascot. All peptides analyzed are shown in Table S5. Deuterium incorporation levels were quantified using HD examiner software (Sierra Analytics), and the quality of every peptide was checked manually. Results are presented as the percentage of maximal deuteration compared to theoretical maximal deuteration. Changes in deuteration level between the two states were considered significant if >15% and >1.5 Da and $p < 0.01$ (unpaired t-test). The mass spectrometry proteomics data have been deposited to the ProteomeXchange Consortium via the PRIDE (*88*) partner repository with the dataset identifier PXD040499 and 10.6019/PXD040499.

## AP-1 reporter assay

HEK293T cells were maintained in DMEM medium (DMEM) supplemented with 10% (v/v) FBS (Thermo Fisher) at 37 °C and 5% $CO_2$. According to the manufacturer's protocol, the AP-1 firefly luciferase reporter vector and the constitutively expressing *Renilla* luciferase vector (BPS Bioscience #60612) were transiently co-transfected together with MKK6$^{DD}$ mutants and p38α pcDNA3.1 plasmids (or empty vector for controls) with Lipofectamin2000 (Thermo Scientific) (Fig. S15). Firefly and *Renilla* luciferase activities were measured 24h post-transfection using the Dual Luciferase assay system (BPS Bioscience #60683) with a Clariostar microplate reader (BMG Germany). Each experiment was repeated three times (biological replicate) and each time, three transfections per condition were performed (technical replicate), for a total of nine experiments per construct. Each firefly luciferase value was normalised by its corresponding *Renilla* luciferase measure to correct for cell quantity and transfection efficiency. The luciferase activity was expressed relative to the replicate positive control (MKK6$^{DD}$ + p38α) intensity. Statistical analysis on the AP-1 reporter assay was performed using Rstudio. Briefly, normal distribution was tested with a Shapiro Wilck test and variance homogeneity with a Levene's test. To compare the mutants to the control (MKK6$^{DD}$ + p38α), either a Welch t-test or a Wilcoxon rank sum exact test was performed.

## Western blots

For Western blots, 20 µg of total protein was loaded on a Tris-Glycine 4–20 % gradient gel (Invitrogen). Rabbit anti-HA (#3724, Cell Signaling) and mouse anti-myc (#2276, Cell signaling) at 1:1000 dilution were used, respectively, for detection of transfected HA-p38α and myc-MKK6 mutants, whilst mouse anti-α-tubulin antibody (NB100-690SS, Biotchne) at 1:5000 dilution was employed as loading control. Secondary antibodies linked to fluorophores, goat anti-rabbit Alexa 488 and goat anti-mouse Alexa 647 (A-11008 and A32728, Thermo Fisher) were used at 1:10000 dilution. Bands were quantified using ImageLab software (BioRad).

## Mass spectrometry

Purified MKK6$^{DD}$GRA-p38α complexes were complemented with 10 mM ATP. Intact mass was measured on a quadrupole time of flight (Q-TOF) Premier mass spectrometer (Waters/Micromass) coupled to an Acquity UPLC System (Waters Corporation). Solvent A was water, 0.1% formic acid, and solvent B was acetonitrile, 0.1% formic acid. Samples were acidified using 1% TFA prior to injection onto an Acquity UPLC Protein BEH C4 column (Waters Corporation). Acquisition was carried out using the standard ESI source in positive ion mode over the mass range 500–3500 m/z. Data were externally calibrated against a reference standard of intact myoglobin, acquired immediately prior to sample data acquisition. Spectra from the chromatogram protein peak were then summed and intact mass was calculated using the MaxEnt1 maximum entropy algorithm (Waters/Micromass).

PTMs were measured by LC-MS/MS. SP3 protocol (*89*) was used for sample preparation. Analysis was performed on an UltiMate 3000 RSLC nano LC system (Dionex) fitted with a trapping cartridge (µ-Precolumn C18 PepMap 100) and an analytical column (nanoEase™ M/Z HSS T3 column 75 µm x 250 mm C18, 1.8 µm, 100 Å, Waters) coupled to a Fusion Lumos (Thermo) mass spectrometer using the proxeon nanoflow source in positive ion mode. Acquired data were processed by IsobarQuant (*90*), as search engine Mascot (v2.2.07) was used.

### Protein structure preparation for MD simulations

The model derived from cryo-EM of p38α in complex with MKK6$^{DD}$GRA was used as a starting conformation for the unbiased MD simulations. The bound ADP that was resolved in the cryo-EM structure was replaced by ATP, which was docked to the binding sites of p38α and MKK6 using the Glide software (*91*) (Schrödinger Release 2021-4). In particular, the docked ATP maintained the ADP pose seen in the cryo-EM structures. The same γ-phosphate position was used for the ATP in the binding site of MKK6. The mutated residues S207D and T211D on the resolved MKK6$^{DD}$ were reverted to the WT ones. The K53R mutation was introduced unintentionally when building the model of p38α with the WT KIM, as this was the mutant used in the crystal structure. It is a kinase-dead mutation that stabilizes the protein for structural studies but has no influence on the studies presented here. The structure of the MKK6GRA-p38α produced by the aforementioned procedure was then used to model the N-terminal tail of the WT MKK6 (residues M1-K14 of the MKK6 WT sequence) using the crystal structure of p38α bound to the WT MKK6 KIM *(31)* and with the *automodel* functionality of MODELLER (*92*).

### MD simulations setup

Prior to any simulation, the protonation state of each residue at pH 7.4 was calculated using the PROPKA 3.1 algorithm as implemented in the PlayMolecule web application (*93*), which left all residues in their usual charge states, except for p38α H228, which was double protonated. For all simulated systems, DES-Amber force field was used for the protein as it has been shown to be able to capture the dynamics of protein-protein complexes more accurately than other force fields to this date (*93*). For the ATP coordinated $Mg^{2+}$ ions, optimized Mg force field parameters that yield water exchange on timescales that agree with experiments (*93*) were combined with the protein force field. The Meagher et al. parameterization for ATP (*94*) was used, as these parameters have been benchmarked recently and shown to be able to reproduce the experimentally observed coordination modes of ATP (*95*). Each system was enclosed in an octahedral box with periodic boundary conditions and solvated with TIP4PD water molecules as described in the DES-Amber force field, while $Na^+$ and $Cl^-$ ions were added to reach neutrality at the final NaCl concentration of 150 mM.

The MD simulations were performed using the GROMACS 2021.3 simulation package (*96*) patched with the PLUMED 2.4.1 plug-in (*97*). The energy of the MKK6GRA-p38α and MKK6-p38α systems was minimized using the steepest descent integrator, and the solvated systems were equilibrated afterwards in the canonical (NVT) ensemble for 10 ns, with initial velocities sampled from the Boltzmann distribution at 310 K and a 2 fs timestep. The temperature was kept constant at 310 K by a velocity-rescale thermostat (*98*). The long-range electrostatics were calculated by the particle mesh Ewald algorithm, with Fourier spacing of 0.16 nm, combined with a switching function at 1.0 nm for the electrostatic and VdW interactions. The systems were then equilibrated for additional 10 ns in the isothermal-isobaric (NPT) ensemble prior to the production runs applying position constraints only to the protein (with a restraint spring constant of 1000 kJ $mol^{-1}$ $nm^{-2}$), where the pressure was maintained at 1 bar through a cell-rescale barostat (*99*).

Post equilibration, we ran a series of independent production runs in the NPT ensemble, coupled with a velocity-rescale thermostat (*92*) at 310 K and a cell-rescale barostat (*99*) at 1 bar for each of the systems as detailed in Table S6. Both unrestrained and restrained sets of replicas for MKK6GRA-p38α are randomly initialized from the same initial conformation and differ by the application of a harmonic restraint on the distance to the native inter-kinase contact found at the interface of the two monomers to maintain the initial relative position of p38α and MKK6GRA.

The distance to the native contact map as implemented in the PLUMED plug-in was restrained using a force constant of 1,500 kJ $mol^{-1}$ $nm^{-2}$. Since the movement of the A-loop of p38α was important, contacts that involved residues of the A-loop were removed from the final contact map. The definition of the atoms involved in each contact, as well as the parameters for the contact map can be found in the input files deposited in the YARETA repository *(66)*. We expanded the dataset of unrestrained simulations for MKK6GRA-p38α adding a set of three replicas starting from a conformation that originates from a snapshot of one of the restrained simulations in which the A-loop of p38α extended towards MKK6 ATP binding site and p38α Y182 was close to MKK6 ATP.

Adaptive MD simulations setup

To better understand how MKK6 engages with p38α, we ran a series of adaptive MD simulations *(49)* that allowed us to extend our sampling of prebound and bound states. This approach has been used in the past to study the association kinetics of small proteins *(50)*. To generate a series of starting conformations for the adaptive simulations, we started by running a 60 ns long adiabatic bias simulation (*100*) for each system (MKK6GRA-p38α, MKK6-p38α) to pull the centres of mass of the two kinases 6 nm apart. In these simulations, a time-dependent harmonic biasing potential with a force constant of 5,000 kJ $mol^{-1}$ $nm^{-2}$ on the centre of mass distance was applied to pull the two kinases away from the conformation seen in the cryo-EM structure. During the course of these simulations, we also applied a harmonic constraint with a force constant of 1,500 kJ $mol^{-1}$ $nm^{-2}$ on a contact map of the KIM with p38α to prevent KIM from unbinding from p38α after the breaking of the N-to-N and C-to-C lobe interfaces. At the end of the adiabatic bias simulations, we manually selected eight conformations for each system representing intermediate states of the detachment process. These conformations were then fed into the adaptive sampling pipeline.

The adaptive method for the MD simulations we ran was based on the following scheme using a GROMACS implementation of the adaptive algorithm found in HTMD (*101*). We subjected each of the starting conformations to an independent 50 ns long unbiased simulation. Then, we retrieved the simulations and analysed them using a Markov state model. From this analysis, we extracted a new set of starting conformations, which were used for the next epoch of parallel simulations, etc. The method with which the conformations for each epoch are selected is the key to speeding up the sampling. After the first epoch, the next epochs use the Markov model to select the next starting conformations. This approach favors the exploration of new and under-sampled states. This strategy can yield large speed-ups compared to non-adaptive MD runs because slow processes with large energy barriers are broken down into steps with individually smaller barriers that can be sampled efficiently. Although the individual simulations are not started from an equilibrium distribution and are shorter than binding and dissociation timescales, Markov modelling approaches can combine such a trajectory ensemble towards unbiased equilibrium models of the long-timescale kinetics and thermodynamics.

For the construction of the on-the-fly MSM during the adaptive simulations, different combinations of features were tested. Out of the tested feature combinations, the following features were used for the construction of the MSM that was used to span new simulations from (i) the distance between the OG1 of p38α T180 and PG of MKK6 ATP, as a descriptor of the phosphorylation of T180, (ii) the distance between the OH of p38α Y182 and PG of MKK6 ATP, as a descriptor of the phosphorylation of Y182, (iii) the contact between p38α S32 and MKK6 N89, as a descriptor of the N-to-N lobe interaction, (iv) the contact between p38α Y258 and MKK6 K268, as a descriptor of the C-to-C lobe interaction, (v) the contact between p38α I116 and MKK6

L13, as a descriptor of the KIM-p38α interaction, and (vi) the contact between p38α F129 and MKK6 V7, as a descriptor of the KIM-p38α interaction. Contacts between residues were defined by nearest-neighbor heavy-atom distances <0.4 nm. For the construction of the MSM during the adaptive simulations, the three slowest linear combinations of the relevant contacts were computed variationally by the TICA method (*102*) (lagtime 20 ns), and this space was discretized using *k*-means clustering ($k = 500$). Each epoch ran for 50 ns of unbiased simulation resulting in 9.2 μs to 9.6 μs of accumulated simulation time for the MKK6GRA-p38α, and MKK6-p38α, respectively (Table S8).

Free energy simulations setup

To evaluate the relative stability of MKK6-p38α and MKK6 αG-helix mutant-p38α at the interaction region between MKK6 αG-helix and the hydrophobic pocket in p38α, we ran Multiple-Walkers (MW) metadynamics simulations in the well-tempered ensemble (*103*). Both systems were initialized from the cryo-EM conformation, and the distance with respect to the native contact map at the C-lobe interface and the distance between the centers of mass of p38α and MKK6 αG-helix (MKK6: residues 264-272, p38α: residues 228-240) were used as collective variables (CVs). The contact map was defined based on the resolved cryo-EM structure considering the sum of the contacts formed between each residue at the C lobes and its neighboring ones within a radius of 0.5 nm. A force constant of 1,500 kJ $mol^{-1}$ $nm^{-2}$ was applied to the distance to the native contact map found at the interface of MKK6 KIM and p38α and at the N-to-N lobe interface to maintain the initial relative position of the two monomers while biasing the detachment at the C-to-C lobe interface. Harmonic restraints were also added to the two CVs to help convergence. The metadynamics simulations were terminated when an extensive exploration of the CV space was achieved. We used 8 walkers in the NPT ensemble and accumulated a simulation time of 2.9 μs and 2.5 μs for MKK6-p38α and MKK6 αG-helix mutant-p38α systems, respectively. The free energy profiles were reconstructed using the instantaneous metadynamics bias shifted by the c(t) factor, and block analysis was performed to compute the statistical error. The simulation parameters used in the metadynamics simulations were the same as the ones used in the unbiased MD simulations.

MD simulations derived structures and analysis

To quantify the rotation of p38α with respect to MKK6 over the course of the simulations, we started by clustering the conformations derived from each MD simulation run. All the conformations visited during each simulation were clustered using the *gromos* algorithm (*104*) and the *g_cluster* routine (GROMACS) by using the RMSD of the backbone atoms of MKK6 as the distance between the structures and the cut-off value from 2 to 4.5 Å to ensure a representative number of frames in each cluster. The central structures of the most populated clusters of each basin (i.e. the structure with the smallest RMSD distance to all the other members of the cluster) were chosen as the representative ones of each simulation. The central structures of each simulation were then superimposed to the cryo-EM structure using the MKK6 as a reference and the rotation matrix of p38α was calculated through the ChimeraX functionalities.

For the kinetic-based clustering, we used all the simulations of each system where no constraints were applied (Table S8) since such constraints could slow down or accelerate certain transitions and affect the population of the resulting clusters. The MD data of each system was projected on the same feature space as the one used during the adaptive sampling (see above). The dominant four time-lagged independent (TICA) components, which represent the most slowly changing collective coordinates in the feature space were then calculated (lagtime 35 ns). The reduced space was used for cluster discretization into microstates with *k*-means clustering (*k*=500). Using the PCCA+ spectral clustering algorithm (*105*), we built a coarse-grained kinetic model by optimally grouping together the fast-mixing microstates resulting from the *k*-means clustering into metastable states.

Since the conformational ensembles that we obtained from all the unbiased MD simulations prior to any clustering are broad and the experimental data often have low information content and may be noisy, we used a Bayesian inference method and the maximum entropy principle framework to refine computationally-derived structural ensembles through experiments. In this framework, an ensemble generated using a prior model is minimally modified to match the experimentally observed data better. In particular, here, we combined ensemble averaged experimental SAXS data with the ensemble of conformations that we obtained after the kinetic clustering with the aim of obtaining a structural ensemble of the system, which agrees with the experimental data. We used an iterative Bayesian/Maximum Entropy (iBME) protocol *(51)(106)*, which takes as input simulations that were generated without taking the experimental data into account, and subsequently updates them using statistical reweighting. The purpose of the reweighting is to derive a new set of weights for each configuration in a previously generated ensemble so that the reweighted ensemble satisfies the following two criteria: (i) it matches the experimental data better than the original ensemble and (ii) it achieves this improved agreement by a minimal perturbation of the original ensemble.

To do so, we first calculated the SAXS profiles of each conformer of the ensemble using the Pepsi-SAXS algorithm (*107*), keeping the scale and background parameters fixed ($I(0) = 1$, $cst = 0$) and and setting the $\delta_\rho$=3.34 e/nm$^3$ (1% with respect to the bulk solvent) and $r_0 = 1.681$ Å. The chosen values of the $\delta_\rho$ and $r_0$ parameters have been shown to give results that approximate well experimentally observed values for most folded proteins *(51)*. To obtain the optimal θ for each ensemble, MKK6$^{DD}$GRA + p38α$^{WT}$ + ADP + $AlF_4^-$ and MKK6$^{DD}$GRA + p38α$^{WT}$ + AMP-PCP, we performed a series of iBME runs with different θ values and selected the θ value that corresponds to the elbow of the $N_{eff}$ vs $\chi^2$ plot (Fig. S12D), as described in (*108*, *109*), using the *kneed* algorithm for the elbow detection. After optimizing the θ parameter (θ=80) for both ensembles, we optimised the weights, *I(0)* and *cst* using iBME against the experimental SAXS curves (Fig. S2) and obtained the ensemble with the best $\chi^2$.

We also repeated the analysis using a synthetic ensemble in which we included calculated SAXS curves associated with the monomers of the kinases. The resulting fit was worse, with a higher $\chi^2$ and the conformations associated with the monomers were zero weighted through iBME, indicating that the SAXS sample did not include monomers. This was expected given that the sample was purified by SEC prior to data collection.

To better characterise the conformations seen in p38α-MKK6GRA state A (Fig. 4, Movie S6), we clustered the ensemble using *k*-means clustering. We used the elbow method to identify the optimal number of clusters (*k*=3). We performed clustering based on the backbone RMSD of the MKK6GRA and p38α cores with respect to the cryo-EM structure (PDB-8A8M) and a conformation extracted from one of the unrestrained MD simulations, where p38α N-lobe is rotated, and T180 approaches MKK6 ATP (see main text).

## Supplementary Text

### Unrestrained simulations of MKK6-p38α indicate that Y182 can reach MKK6 ATP

Since the resolved cryo-EM structure has a chimeric MKK6 with a modified KIM on its N-terminal tail adopted from GRA24, we reasoned that the simulations of the MKK6-p38α with the WT KIM of MKK6 could give us more information on the role of this motif that the cryo-EM structure alone could not provide. In the WT, the “electrostatic hook” of KIM is recognised by p38α and forms ion pairs with residues of the β7/β8 turn of p38α. Indeed, during the simulations, K8 and R9 of the WT sequence anchor the KIM to p38α by forming backbone and side-chain hydrogen bonds and salt-bridges with E161, while the salt-bridge between the side chains of K14 and E160 further solidifies the KIM around p38α (Fig. S16). Unlike the set of simulations with the chimeric MKK6, in two out of the five simulations of this setup, we see both T180 and Y182 coming relatively close to MKK6 ATP (Table S9) without p38α having to rotate. Both during the approaching of the A-loop of p38α to the MKK6 ATP and after, the two kinases maintain their initial relative orientation throughout the simulations.

During the simulations of p38α with MKK6 comprising of the WT sequence, we were not able to see the rotation of p38α even though T180 got relatively close to ATP in one of the replicas. We think that the simulation time may not be sufficient for the N-lobe of p38α to rotate.

### Restraining the MKK6GRA-p38α relative position enhances the phosphorylation at Y182

We ran a set of five simulations for the MKK6GRA-p38α dimer, starting from the cryo-EM structure and applying mild harmonic restraints on the interface interactions to stabilise the relative orientation of the monomers in the complex (see Methods). Due to the presence of the restraints, we did not observe any large conformational change akin to the one seen in the unrestrained simulation described in the Main Text, showing T180 clearly interacting with MKK6 ATP.

In this set of restrained simulations, two out of the five replicas show p38α A-loop adopting an extended conformation with Y182 approaching $P_\gamma$ of MKK6 ATP up to a final distance of 4.4 Å and 3.5 Å, respectively. In both cases, p38α ATP binding site slightly opens allowing the adenine group of p38α ATP to move out of the binding site. Interestingly, in one of the two simulations, we also see that the extended A-loop forms a one-turn helix (residues E178-Y182), which involves both phosphorylation sites. A similar transient helix on the middle section of the A-loop, which exposes the phosphorylation sites, has been reported in MD simulations of the unphosphorylated kinase domain of EGFR (*110, 111*), and is also reminiscent of a helix in the A-loop of MPSK1 kinase (*112*) (PDB-2BUJ). In the rest of the replicas of this set of simulations, the conformation adopted by the A-loop is not compatible with phosphorylation on either T180 or Y182 since the A-loop extends towards the p38α C-lobe or the MKK6 αC-helix.

It is worth mentioning that in all restrained simulations, the KIM never detaches from p38α regardless of the relative conformation – catalytically compatible or not – adopted by the two kinases.

### Released simulations of MKK6GRA-p38α confirm the role of MKK6 KIM in stabilising the active complex

The results obtained from the set of restrained simulations suggest a role of MKK6 KIM in stabilizing the MKK6-p38α complex. However, due to the presence of the harmonic restraints on the interface contacts, we were not able to evaluate to what extent MKK6 KIM contributes to the rotation of the p38α N-lobe.

We thus ran an additional set of three simulations releasing the restraints on the interface. We started the simulations from a representative conformation of the complex extracted from one of the restrained simulations showing Y182 pointing towards the MKK6 ATP (Y182-$P_{\gamma}$=5.1 Å) and residues E178-Y182 of the A-loop folded into a one-turn helix.

In two out of three replicas the KIM remains stably in contact with p38α throughout the simulation.

Concurrently, we observe that in one simulation, p38α A-loop extends above the MKK6 αC-helix in a way that allows Y182 to interact with Q93, forming, thus, a catalytically incompatible complex. In the simulation we extended up to 2 μs, we observed the unfolding of the one-turn helix of the A-loop and T180 approaching MKK6 ATP. After clustering of this trajectory (RMSD cut-off distance equal to 2.75 Å), in the most populated cluster (cluster 1), Y182 and T180 fluctuate at 1-2 nm away from MKK6 ATP while in the second most populated cluster (cluster 2) they reach at a distance <1 nm. Interestingly, in cluster 1, the p38α N-lobe is turned by approximately 51° with respect to the initial conformation, while in cluster 2, in which both Y182 and T180 are closer to MKK6 ATP, the rotation is more significant, i.e., approximately 66°. This observation is consistent with what we observed with the unrestrained simulation showing the N-lobe having to rotate for T180 to interact with MKK6 ATP. Although interesting, from this simulation we were not able to confirm the role of the salt bridge between MKK6 K17 and p38α E160 in priming the rotation of p38α.

Lastly, in the third simulation of this set, we observed p38α A-loop moving from an extended to sequestered conformation concurrently with the dissociation of MKK6 KIM, thus confirming the role of MKK6 KIM in stabilizing the active complex. The conformational change of the A-loop required approximately 200 ns after the detachment of the KIM. Finally, even when most interface contacts are lost, the contacts around the hydrophobic patch between the C-lobes of p38α and MKK6 are maintained. Comparing the complex conformation with a reference structure for inactive p38α (PDB-3S3I) we were able to assess the inactive-like conformation of the A-loop adopted at the end of the simulation ($RMSD\,{}^{p38\alpha}_{backbone}$= 3.5 Å with respect to the crystal structure, Fig. S11). The KIM is also in contact with the hinge region of p38α. It is worth mentioning that during the simulations that we ran, we see that fluctuations of MKK6 are propagated through its N-terminal loop and KIM to the hinge region of p38α, affecting the stability of p38α ATP inside its pocket.

### p38α-MKK6 αG-helix mutant populates conformations showing a detached C-to-C-lobe interface

We performed multiple-walkers metadynamics simulations to assess the relative stability of p38α in complex with MKK6 and MKK6 αG-helix mutant. Specifically, we biased the distance between the centres of mass of p38α and MKK6 αG-helix to enhance the separation of the complex and the distance to the native contact map at the C-to-C-lobe interface. By reconstructing the free energy surface underlying the detachment of the complex at the C-lobe interface, we were able to quantify the relative stability of the two complexes. In Fig. S9C, we reported the free energy profiles as a function of the distance to the native contact map of the cryo-EM structure at the C-lobe interface for both systems. The free energy surface of p38α-MKK6 αG-helix mutant indicates that the detached conformation at the C-to-C-lobe interface (contact map distance > 20 a.u.) is more populated than the conformation observed in the cryo-EM structure (Fig. S9D). Conversely, the p38α-MKK6 complex populates conformations showing the C-lobes interacting with each other at the hydrophobic patch as seen in the cryo-EM structure (contact map distance < 20 a.u., Fig. S9D).

These results agree with the biochemical data (Fig. 2F) and the HDX data (Fig. S9B), which show reduced activity in the presence of the αG-helix mutations and no shielding of p38α in the MAPK insert region by the MKK6$^{DD}$αG-helix mutant.

## Kinetic clustering of the p38α-MKK6 WT reveal intermediate states

Similar to the MKK6GRA-p38α, one of the clusters of MKK6-p38α corresponds to the face-to-face conformation, and the A-loop of p38α adopts a conformation that brings T180 and Y182 close to the MKK6 ATP (state F, Movie S11). However, unlike the MKK6GRA-p38α, we do not see the rotated p38α in this ensemble. The second macrostate is again similar to state B of MKK6GRA-p38α in which the p38α A-loop has a conformation similar to the one seen in the cryo-EM structure, but the N-to-N lobe interaction is lost (state G, Movie S12). Finally, apart from the state that corresponds to the non-specific binding of MKK6 (state H, Movie S13), we see again a late intermediate state in which the KIM is bound to its recognition site while the N-lobes are separated (state J, Movie S14), reminiscent of a tightly bound state. Figure S13 displays all the macrostates that were identified for the MKK6-p38α.

## Conformations seen within the face-to-face macrostate of MKK6GRA-p38α

Clustering of the conformations in the catalytically relevant state A of MKK6GRA-p38α (Fig. 4, Move S6) showed the presence of three distinct conformations. In particular, these conformations correspond to the face-to-face cryo-EM structure, the N-lobe rotated p38α, and an intermediate conformation where the two kinases are held together by the C-to-C lobe interface and the N-lobe of p38α is not fully rotated yet.

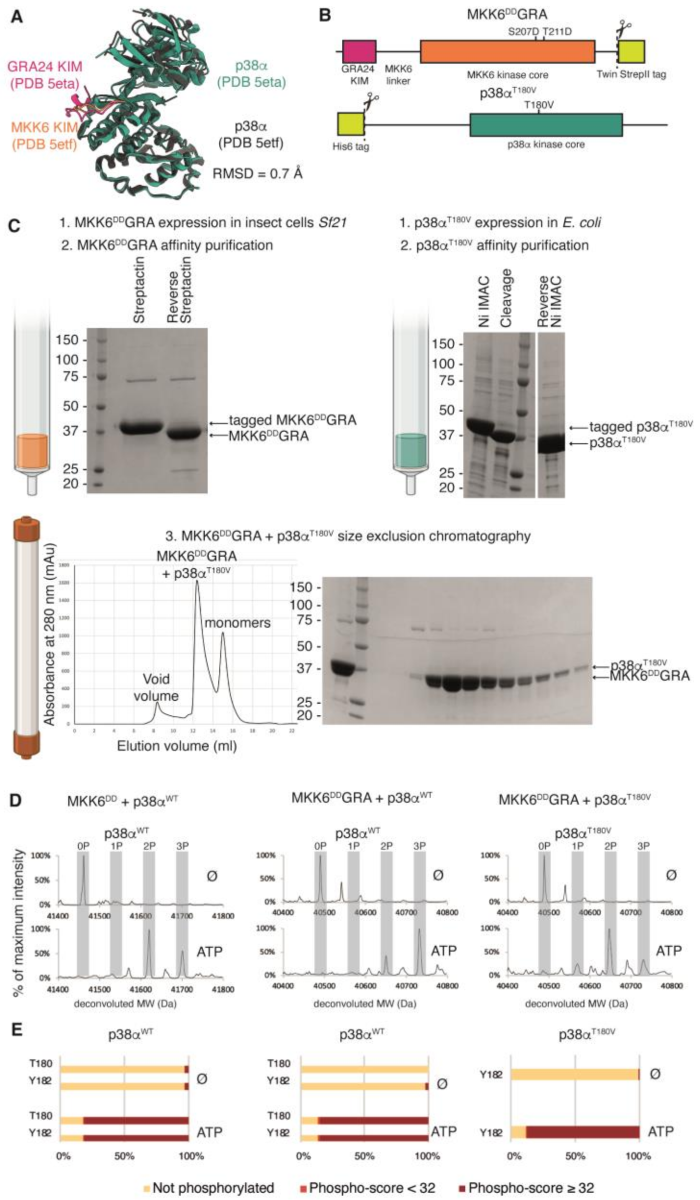

**Fig. S1. Expression, purification and activity of the MKK6$^{DD}$GRA-p38α$^{T180V}$ complex.** (**A**) The *Toxoplasma* GRA24 KIM induces the same conformational change on p38α as the native MKK6 KIM, despite having higher affinity. The RMSD between the MKK6 KIM – p38α crystal structure (PDB 5etf) and the GRA24 KIM – p38α crystal structure (PDB 5eta) is 0.7 Å. (**B**) Constructs of MKK6$^{DD}$GRA and p38α$^{T180V}$ used for structural studies. (**C**) MKK6$^{DD}$GRA and p38α$^{T180V}$ were respectively expressed in *Sf21* and *E. coli*. They were purified by affinity purification (StrepTactin and Ni IMAC, respectively), followed by cleavage with 3C protease, and reverse affinity purification. Both proteins were mixed, and the complex was purified with size-exclusion chromatography. (**D-E**) Mass spectrometry (Native ESI-QTOF in (**D**) and LC-MS/MS in (**E**) reveals that the MKK6$^{DD}$GRA chimera can phosphorylate p38α$^{WT}$ as the MKK6$^{DD}$ construct, as well as p38α$^{T180V}$. In the presence of ATP, several sites on both proteins are phosphorylated, including both T180 and Y182 residues of p38α$^{WT}$ A-loop and Y182 residue of p38α$^{T180V}$ A-loop.

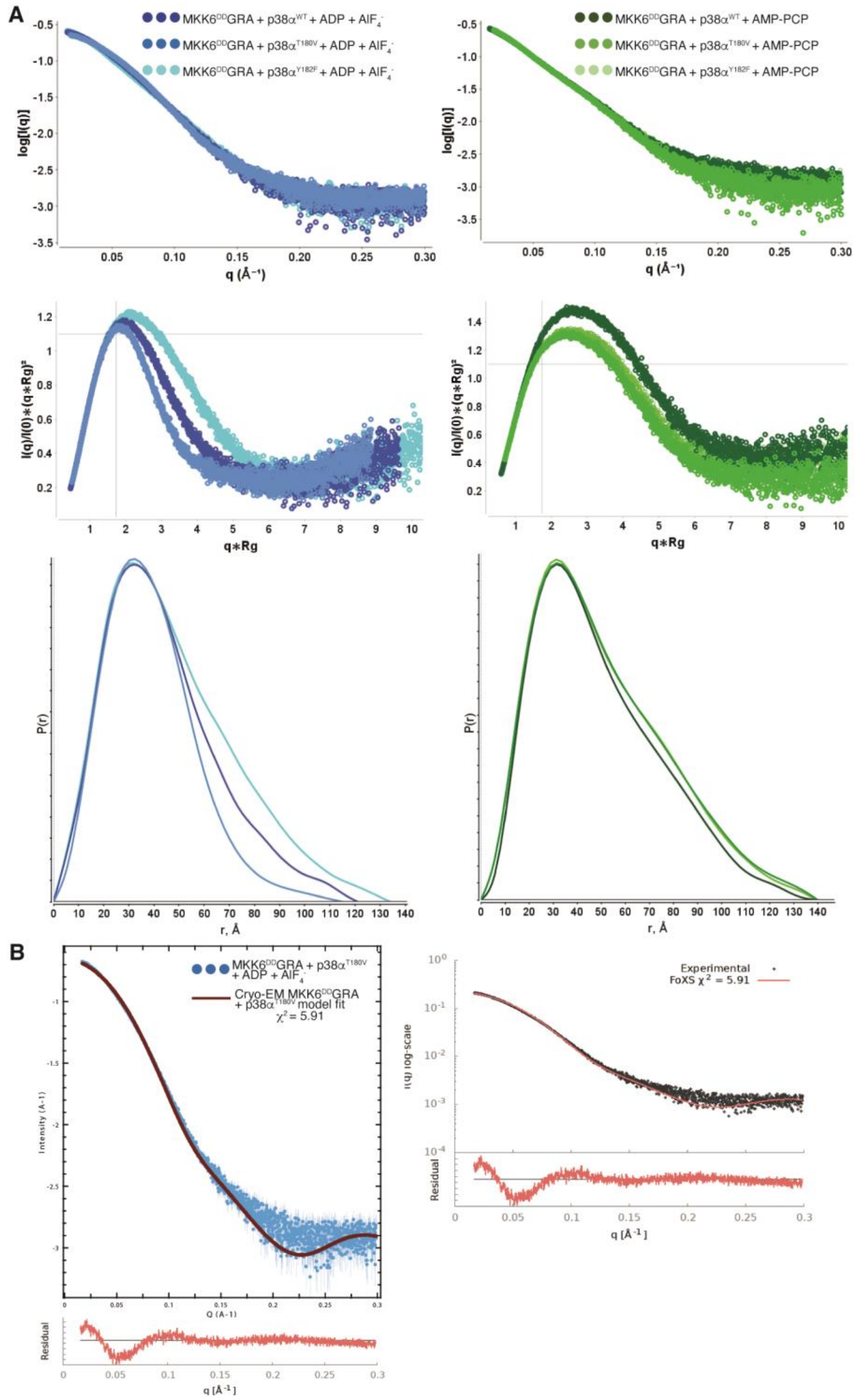

**Fig. S2. SAXS curves for MKK6$^{DD}$GRA + p38α mutant complexes.** (**A**) The blue panels show the IvsQ, Kratky, and P(r) plots for MKK6$^{DD}$GRA + p38α mutants + ADP + AlF$_4^-$ complexes. The complex with p38α$^{T180V}$ mutant is more compact than the one with p38α$^{WT}$, which is more compact than the one with p38α$^{Y182F}$ mutation. The green panels are the same plots for the MKK6$^{DD}$GRA + p38α mutants + AMP-PCP complexes. The complex with p38α$^{WT}$ has a slightly increased Rg compared to the two mutant ones, but all share a similar D$_{max}$. (**B**) $\chi^2$ fits for the cryo-EM MKK6$^{DD}$GRA + p38α$^{T180V}$ model (brick).

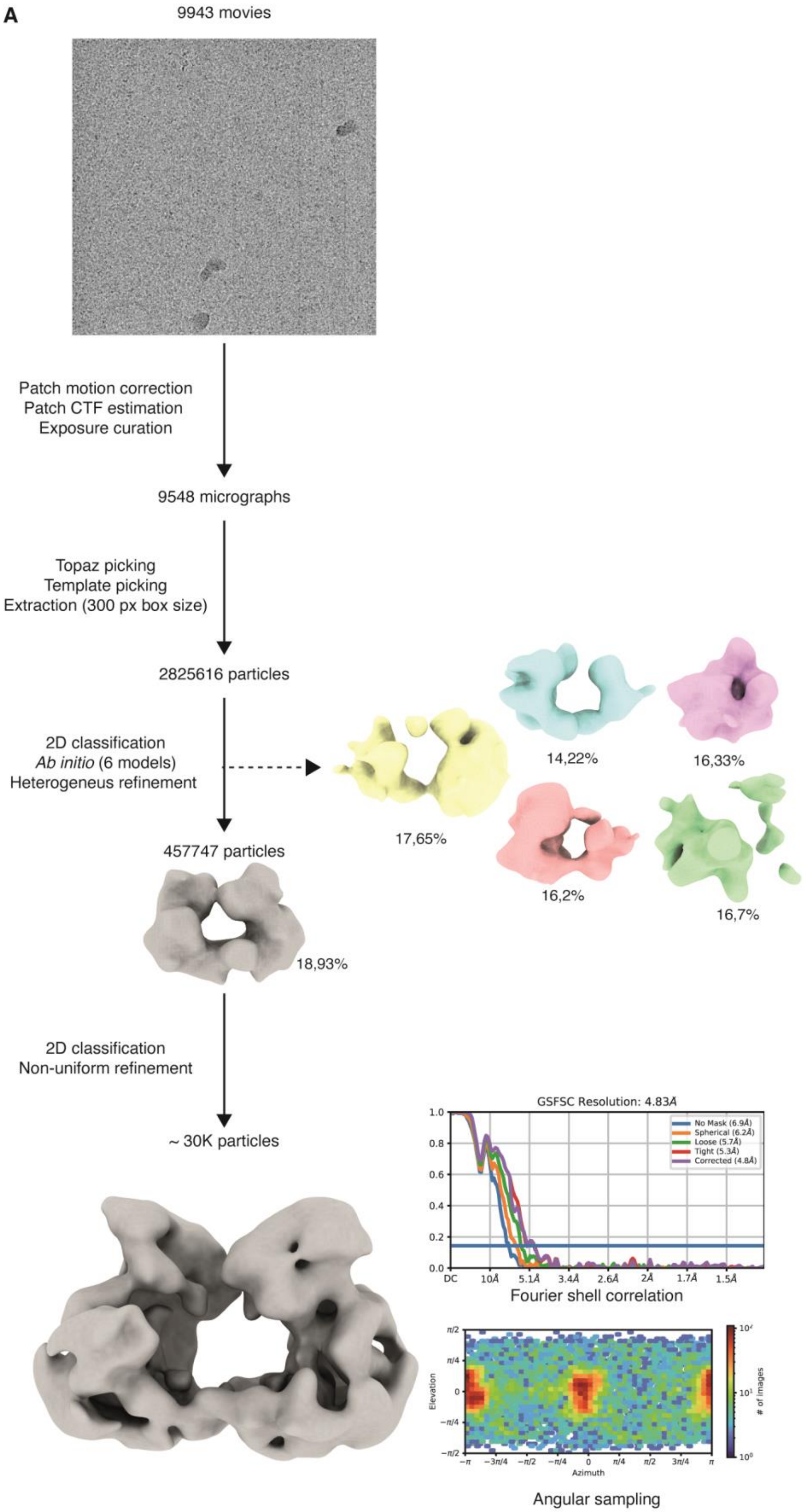
A
9943 movies
Patch motion correction
Patch CTF estimation
Exposure curation
9548 micrographs
Topaz picking
Template picking
Extraction (300 px box size)
2825616 particles
2D classification
*Ab initio* (6 models)
Heterogeneous refinement
14,22%
16,33%
17,65%
16,2%
16,7%
457747 particles
18,93%
2D classification
Non-uniform refinement
~ 30K particles
GSFSC Resolution: 4.83Å
No Mask (6.9Å)
Spherical (6.2Å)
Loose (5.7Å)
Tight (5.3Å)
Corrected (4.8Å)
1.0
0.8
0.6
0.4
0.2
0.0
DC
10Å
5.1Å
3.4Å
2.6Å
2Å
1.7Å
1.5Å
Fourier shell correlation
π/2
π/4
0
−π/4
−π/2
Elevation
−π
−3π/4
−π/2
−π/4
0
π/4
π/2
3π/4
π
Azimuth
$10^2$
$10^1$
$10^0$
# of images
Angular sampling

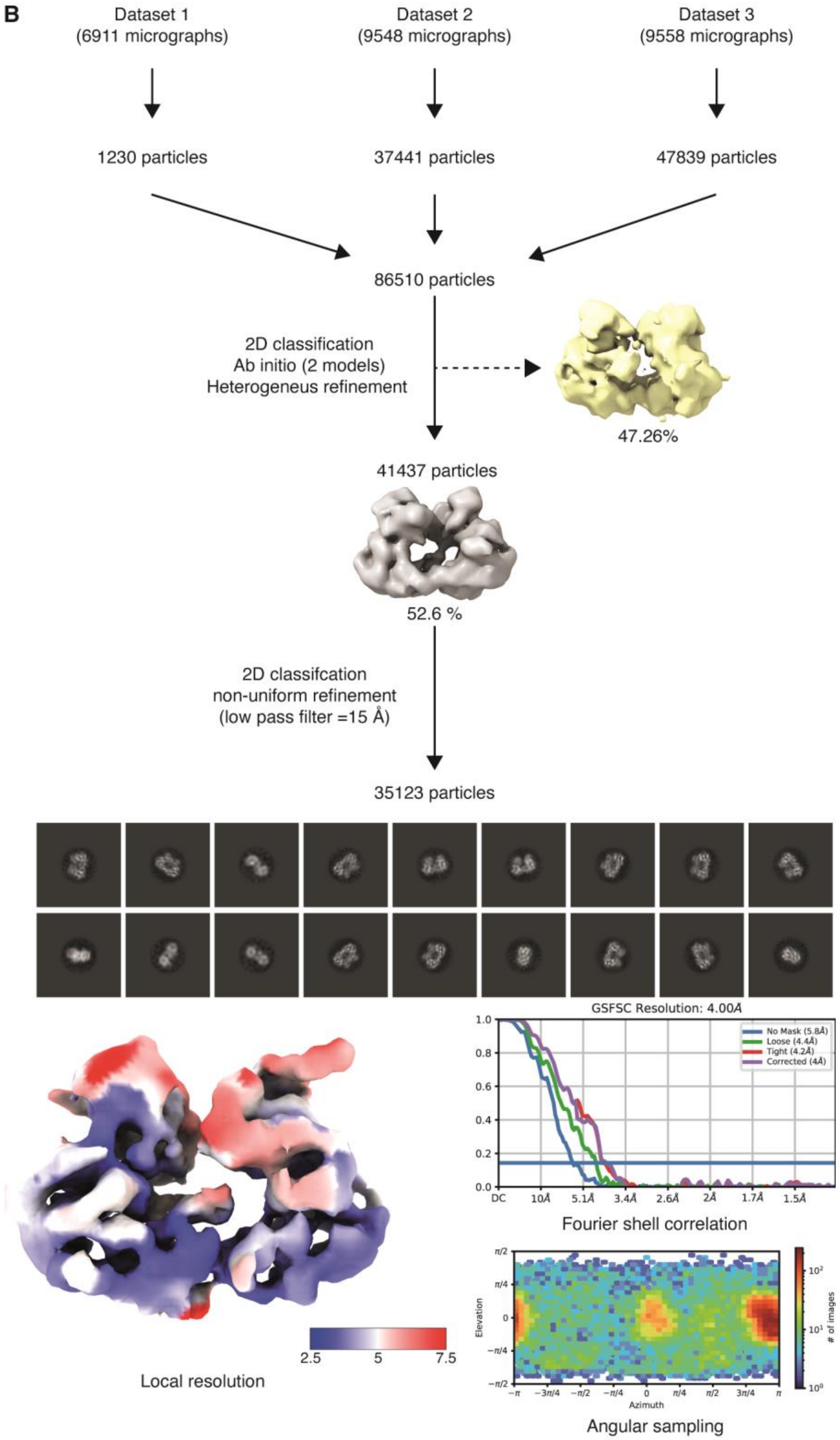
B
Dataset 1
(6911 micrographs)
Dataset 2
(9548 micrographs)
Dataset 3
(9558 micrographs)
1230 particles
37441 particles
47839 particles
86510 particles
2D classification
Ab initio (2 models)
Heterogeneus refinement
47.26%
41437 particles
52.6 %
2D classifcation
non-uniform refinement
(low pass filter =15 Å)
35123 particles
GSFSC Resolution: 4.00Å
1.0
0.8
0.6
0.4
0.2
0.0
DC
10Å
5.1Å
3.4Å
2.6Å
2Å
1.7Å
1.5Å
No Mask (5.8Å)
Loose (4.4Å)
Tight (4.2Å)
Corrected (4Å)
Fourier shell correlation
2.5
5
7.5
Local resolution
π/2
π/4
0
−π/4
−π/2
Elevation
−π
−3π/4
−π/2
−π/4
0
π/4
π/2
3π/4
π
Azimuth
10²
10¹
10⁰
# of images
Angular sampling

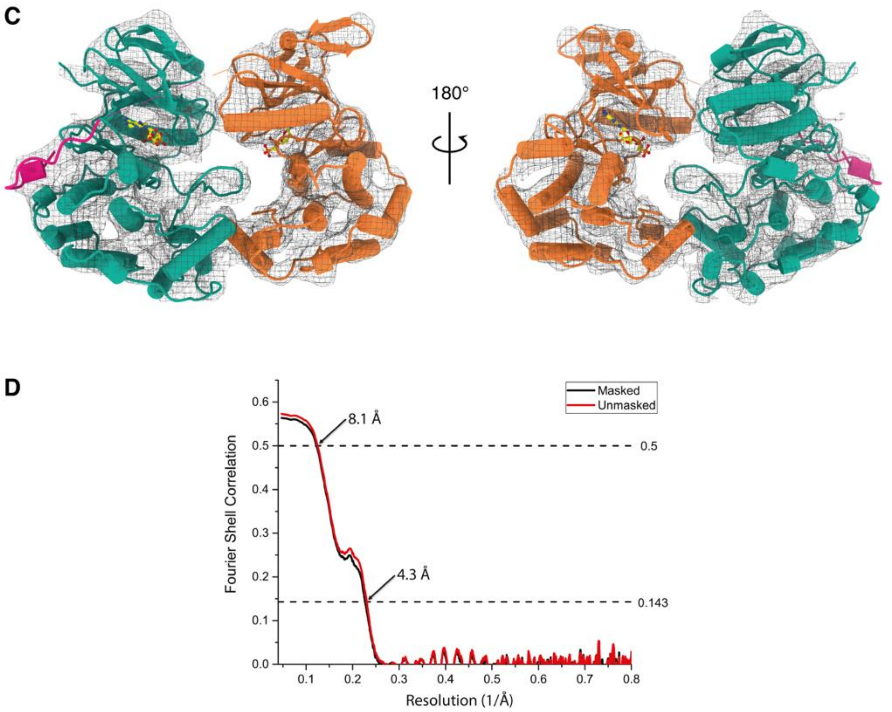

**Fig. S3. Cryo-EM processing and data assessment of the MKK6$^{DD}$GRA-p38α$^{T180V}$ model.** (**A**) Exemplary workflow processing for one of the three datasets collected (dataset 2). Data processing was performed in cryoSPARC. A representative micrograph, typical result from heterogeneous refinement, final map with angular sampling and gold-standard Fourier Shell Correlation are also shown. (**B**) Cryo-EM processing of the final particle selection from the three merged datasets to obtain the final reconstruction at 4.0 Å resolution. Representative 2D classes, which yielded the final map, the final sharpened map, coloured according to local resolution, angular sampling and gold-standard Fourier Shell Correlation (Nyquist = 1.276 Å) are shown. (**C**) Fitting of the model into the cryo-EM map. The MKK6$^{DD}$GRA-p38α$^{T180V}$ complex is shown in cartoon representation with α-helices as cylinders, and the sharpened map is shown as a black mesh. (**D**) FSC between model and cryo-EM maps as a function of spatial frequency (Nyquist = 0.78 Å$^{-1}$)

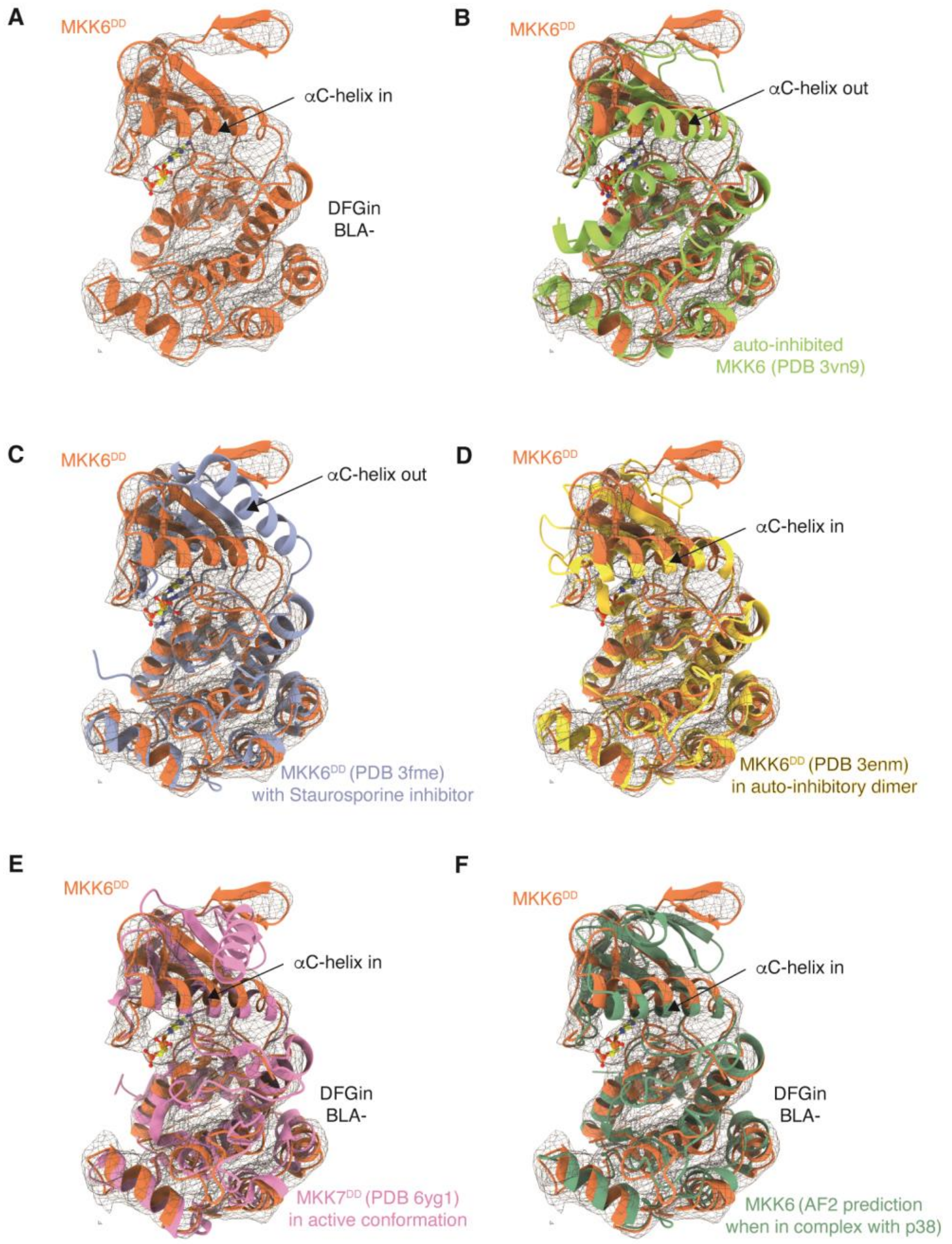

**Fig. S4. Comparison of MKK6 models with the cryo-EM structure.** (**A**) MKK6$^{DD}$ cryo-EM model fitted into the sharpened cryo-EM map (shown as a black mesh). (**B-F**) Overlay of the cryo-EM structure of MKK6$^{DD}$GRA with (**B**) the crystal structure of MKK6 in an inactive conformation with AMP-PNP bound, (**C**) the crystal structure of MKK6 in an inactive conformation inhibited with *staurosporin*, (**D**) the crystal structure of MKK6 in an auto-inhibitory dimer, (**E**) the crystal structure of active MKK7 and (**F**) the AlphaFold2 model of MKK6 when in complex with p38α.

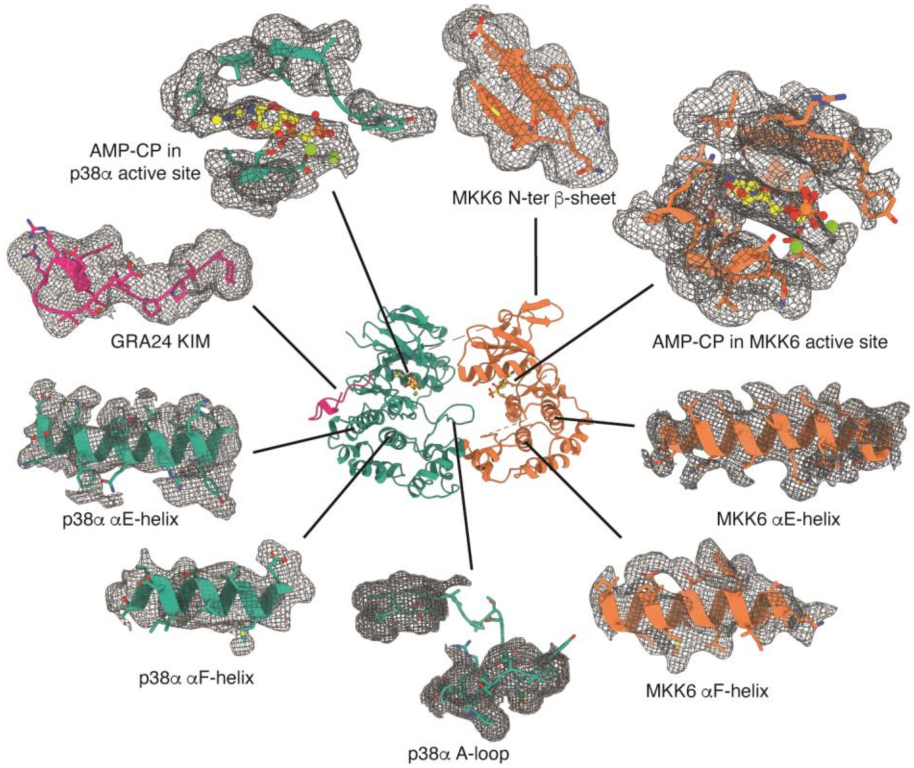

**Fig. S5. Detailed views of the MKK6$^{DD}$GRA-p38α$^{T180V}$ model with the sharpened Coulomb potential map.** Structural elements of the model are shown in cartoon and stick representation and the sharpened map is shown as a black mesh.

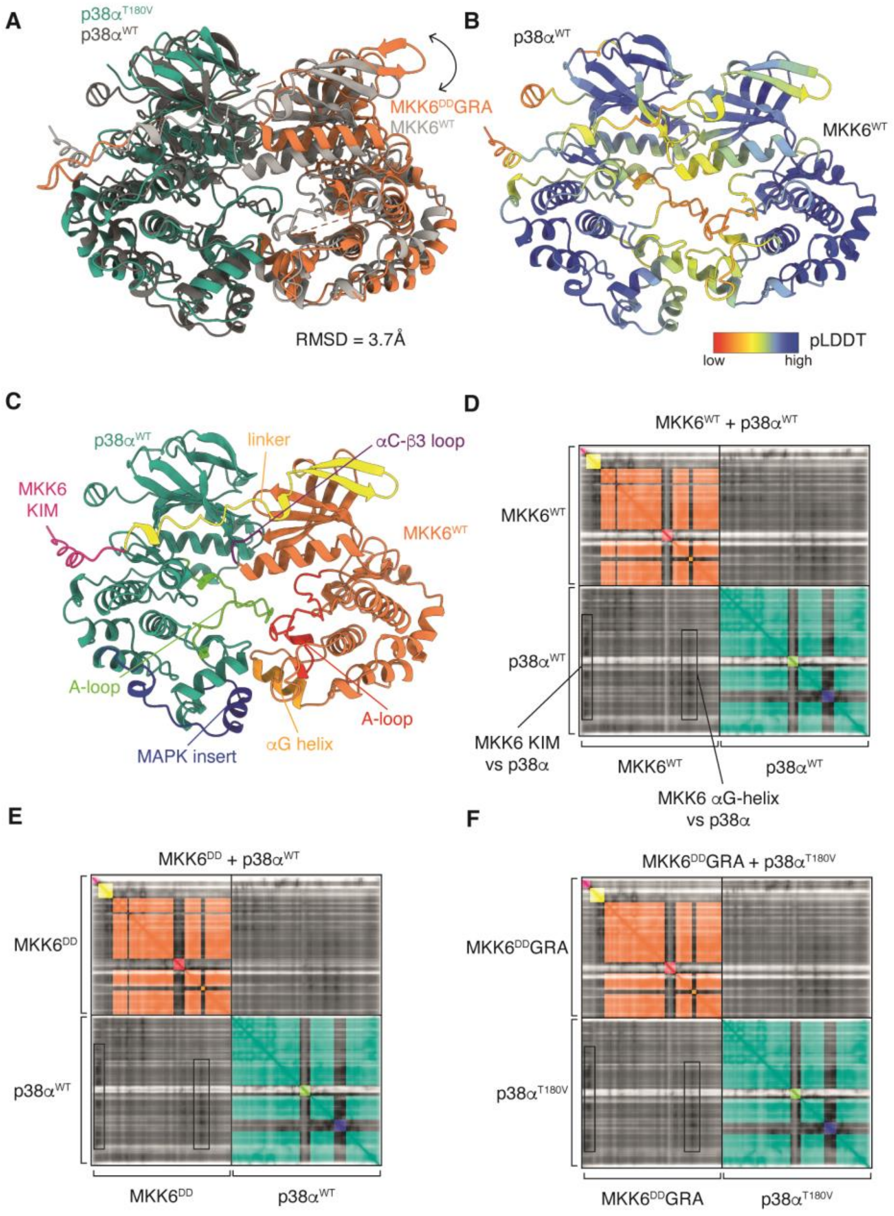

**Fig. S6. AlphaFold2 multimer predicts a similar interface of the complex. (A)** MKK6$^{DD}$GRA-p38α$^{T180V}$ model (colour), superimposed with the AlphaFold2 prediction of the complex (grey). Differences in domain orientation are indicated by arrows and the overall RMSD value of the superposition is indicated. (**B**) Cartoon representation of the MKK6-p38α predicted model, coloured according to its per-residue confidence (pLDDT). (**C**) AlphaFold2 predicted MKK6-p38α model with relevant motifs indicated. (**D**) Predicted Aligned Error (PAE) plots for the MKK6-p38α prediction. Low PAE values (0 to 30 Å, decrease in grey scale) indicate higher confidence in respective residue placement. Within protein domains, PAE values are lowest, however, intermolecular placement, seen in the bottom left and top right quadrants, show confident placement, indicated by dark grey. For orientation, domains and relevant motifs in the plot are coloured as in (**C**). (**E**-**F**) PAE plots for MKK6$^{DD}$GRA-p38α and MKK6$^{DD}$GRA-p38α$^{T180V}$ predictions, respectively, showing similar PAE values at the interfaces between the kinases.

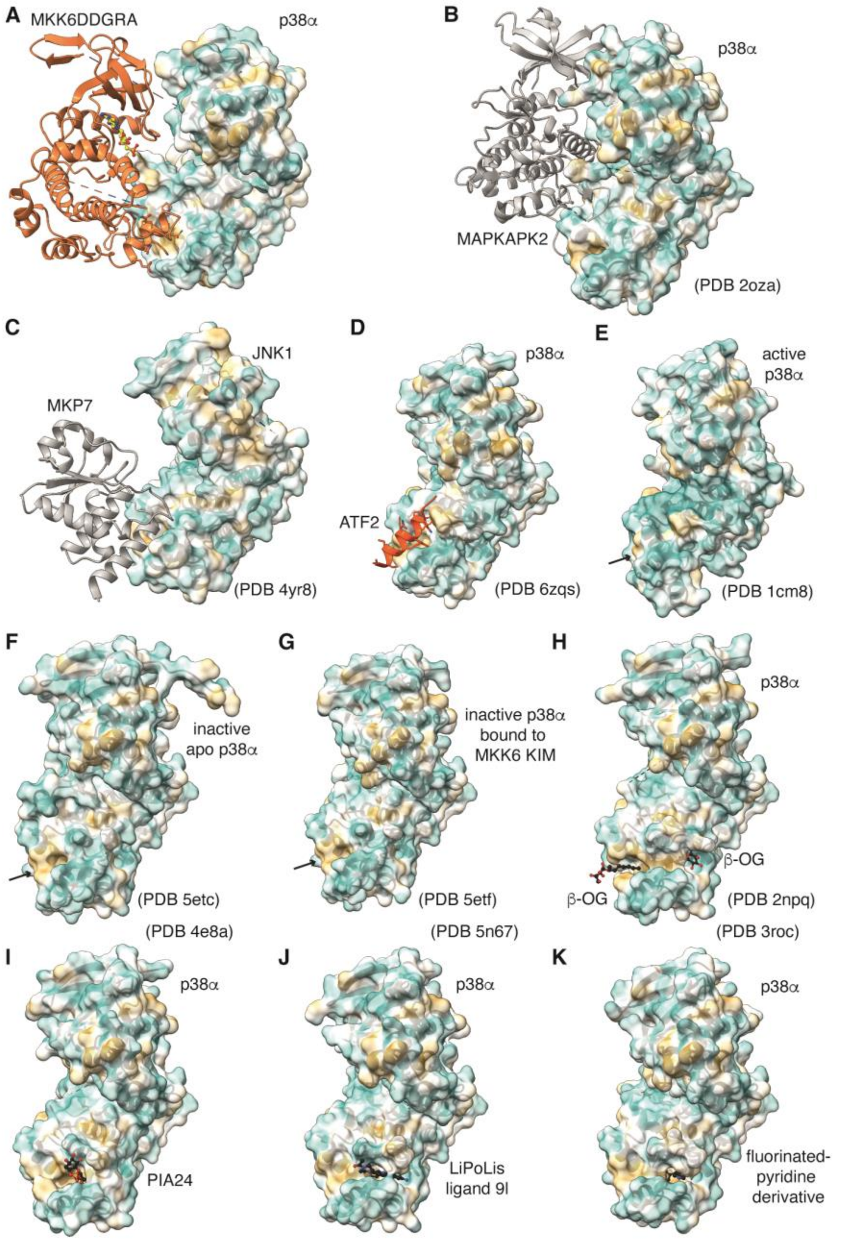

**Fig. S7. Interaction with, and variability of, the p38α hydrophobic pocket.** The p38α surface is colored according to hydrophobicity. (**A**) Cryo-EM MKK6$^{DD}$GRA-p38α$^{T180V}$ model. (**B**) Crystal structure of p38α bound to its substrate MAPKAPK2 in an inactive complex showing a different binding mode. (**C)** Crystal structure of JNK1 bound to MKP7 phosphatase showing a similar binding mode as the MKK6 αG helix. (**D)** Crystal structure of p38α bound to the substrate ATF2 peptide showing a similar binding mode as the MKK6 αG helix. (**E-G**) The p38α hydrophobic pocket is flexible: it is opened in inactive p38α crystal structures and closes in active p38α conformation. (**H-K**) The p38α hydrophobic pocket can bind small molecules and regulatory lipids: (**H**) β-octyl-D-glucopyranoside (β-OG) detergent, (**I**) phosphatidylinositol ether lipid analogue 24 (PIA24), (**J**) LiPoLis ligand 9l, and (**K**) a fluorinated-pyridine derivative.

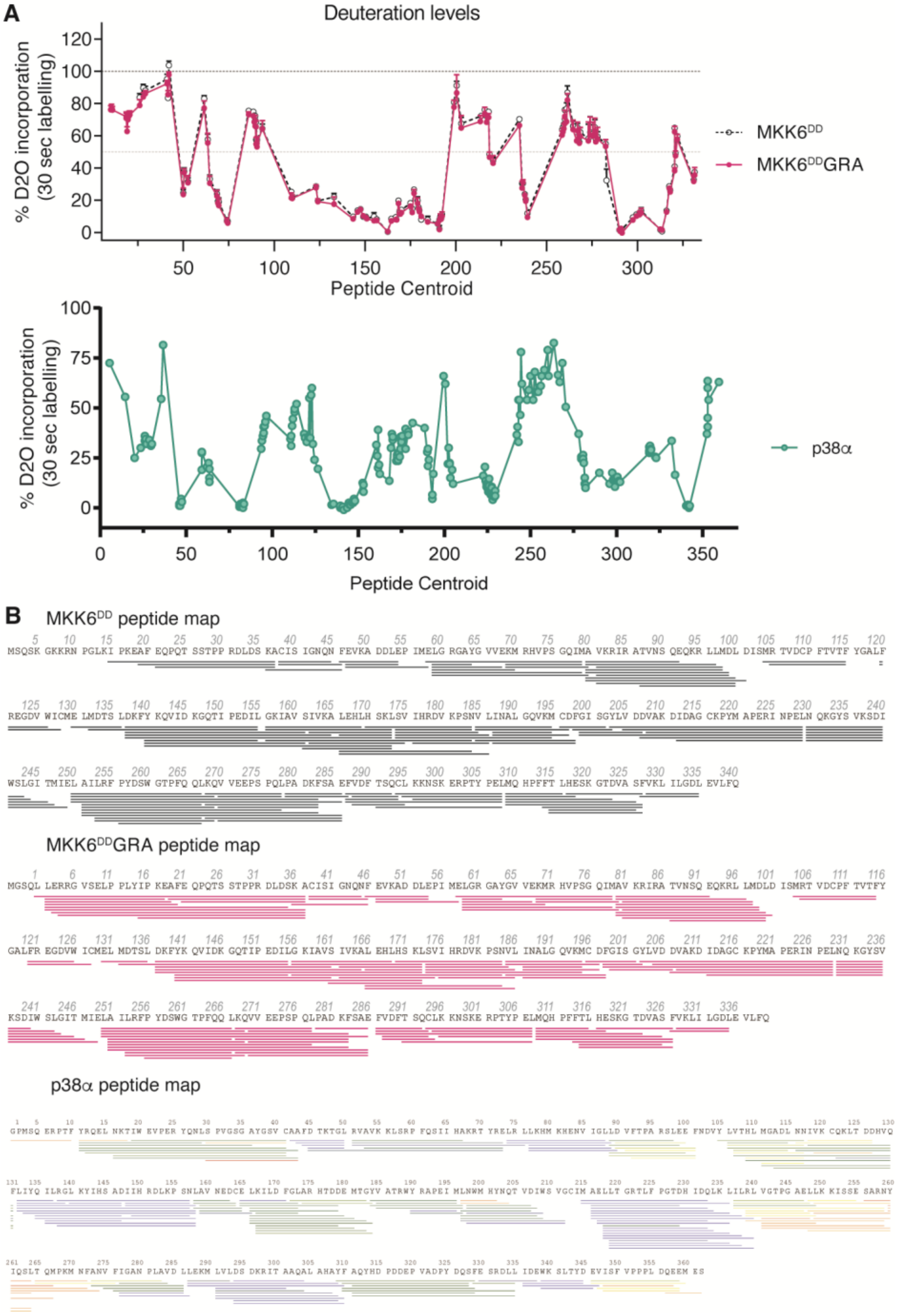
A
Deuteration levels
% D2O incorporation (30 sec labelling)
120
100
80
60
40
20
0
50
100
150
200
250
300
Peptide Centroid
MKK6DD
MKK6DDGRA
% D2O incorporation (30 sec labelling)
100
75
50
25
0
0
50
100
150
200
250
300
350
Peptide Centroid
p38α
B
MKK6DD peptide map
5 10 15 20 25 30 35 40 45 50 55 60 65 70 75 80 85 90 95 100 105 110 115 120
MSQSK GKKRN PGLKI PKEAF EQPQT SSTPP RDLDS KACIS IGNQN FEVKA DDLEP IMELG RGAYG VVEKM RHVPS GQIMA VKRIR ATVNS QEQKR LLMDL DISMR TVDCP FTVTF YGALF
125 130 135 140 145 150 155 160 165 170 175 180 185 190 195 200 205 210 215 220 225 230 235 240
REGDV WICME LMDTS LDKFY KQVID KGQTI PEDIL GKIAV SIVKA LEHLH SKLSV IHRDV KPSNV LINAL GQVKM CDFGI SGYLV DDVAK DIDAG CKPYM APERI NPELN QKGYS VKSDI
245 250 255 260 265 270 275 280 285 290 295 300 305 310 315 320 325 330 335 340
WSLGI TMIEL AILRF PYDSW GTPFQ QLKQV VEEPS PQLPA DKFSA EFVDF TSQCL KKNSK ERPTY PELMQ HPFFT LHESK GTDVA SFVKL ILGDL EVLFQ
MKK6DDGRA peptide map
1 6 11 16 21 26 31 36 41 46 51 56 61 65 71 76 81 86 91 96 101 106 111 116
MGSQL LERRG VSELP PLYIP KEAFE QPQTS STPPR DLDSK ACISI GNQNF EVKAD DLEPI MELGR GAYGV VEKMR HVPSG QIMAV KRIRA TVNSQ EQKRL LMDLD ISMRT VDCPF TVTFY
121 126 131 136 141 146 151 156 161 166 171 176 181 186 191 196 201 206 211 216 221 226 231 236
GALFR EGDVW ICMEL MDTSL DKFYK QVIDK GQTIP EDILG KIAVS IVKAL EHLHS KLSVI HRDVK PSNVL INALG QVKMC DFGIS GYLVD DVAKD IDAGC KPYMA PERIN PELNQ KGYSV
241 246 251 256 261 266 271 276 281 286 291 296 301 306 311 316 321 326 331 336
KSDIW SLGIT MIELA ILRFP YDSWG TPFQQ LKQVV EEPSP QLPAD KFSAE FVDFT SQCLK KNSKE RPTYP ELMQH PFFTL HESKG TDVAS FVKLI LGDLE VLFQ
p38α peptide map
1 5 10 15 20 25 30 35 40 45 50 55 60 65 70 75 80 85 90 95 100 105 110 115 120 125 130
GPMSQ ERPTF YRQEL NKTIW EVPER YQNLS PVGSG AYGSV CAAFD TKTGL RVAVK KLSRP FQSII HAKRT YRELR LLKHM KHENV IGLLD VFTPA RSLEE FNDVY LVTHL MGADL NNIVK CQKLT DDHVQ
131 135 140 145 150 155 160 165 170 175 180 185 190 195 200 205 210 215 220 225 230 235 240 245 250 255 260
FLIYQ ILRGL KYIHS ADIIH RDLKP SNLAV NEDCE LKILD FGLAR HTDDE MTGYV ATRWY RAPEI MLNWM HYNQT VDIWS VGCIM AELLT GRTLF PGTDH IDQLK LILRL VGTPG AELLK KISSE SARNY
261 265 270 275 280 285 290 295 300 305 310 315 320 325 330 335 340 345 350 355 360
IQSLT QMPKM NFANV FIGAN PLAVD LLEKM LVLDS DKRIT AAQAL AHAYF AQYHD PDDEP VADPY DQSFE SRDLL IDEWK SLTYD EVISF VPPPL DQEEM ES

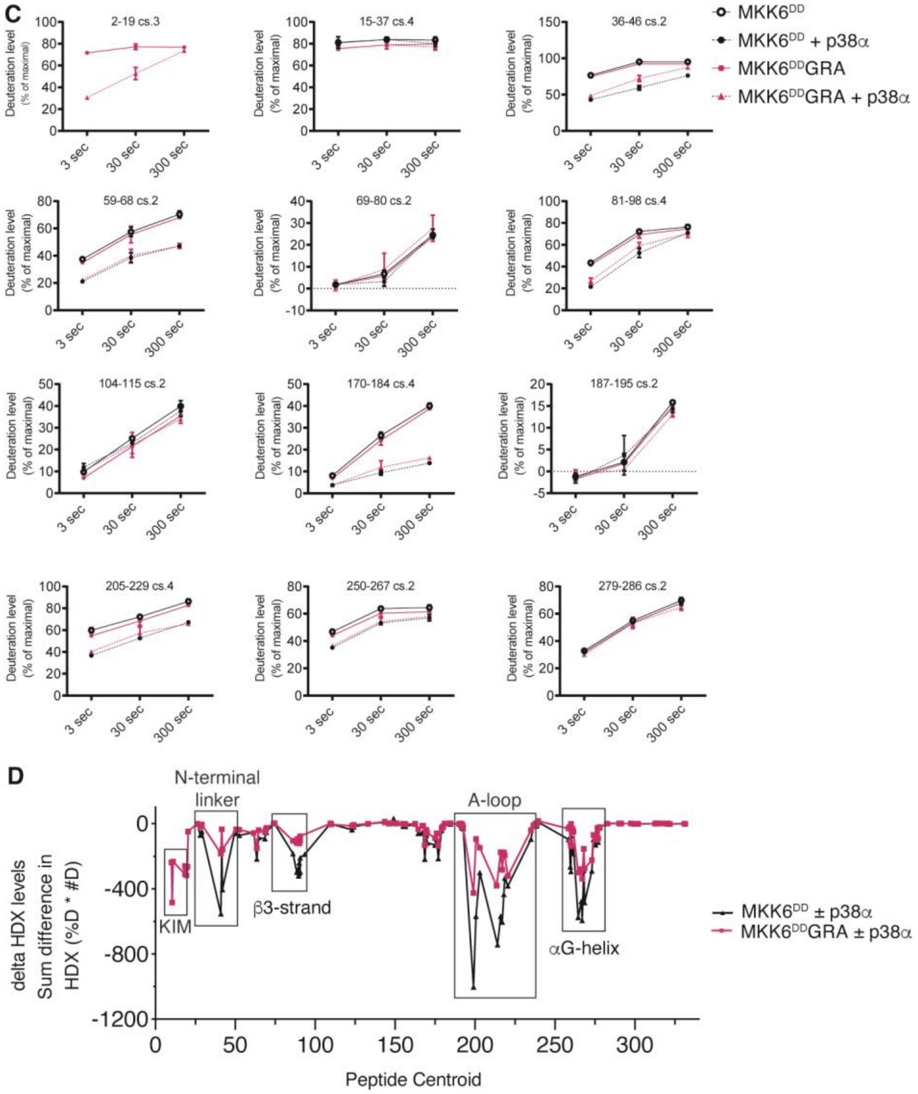

**Fig. S8. HDX-MS shows that MKK6$^{DD}$GRA and MKK6$^{DD}$ bind similarly to p38α** (**A**) Deuteration levels for each peptide of both MKK6$^{DD}$ and MKK6$^{DD}$GRA. Each dot represents one peptide plotted on the x-axis according to the central residue of the peptide (centroid). (**B**) Peptide map for both MKK6 proteins and p38α. Each line represents a high-quality peptide analyzed in this study. (**C**) Uptake plots of a representative selection of peptides. Residue numbering based on MKK6$^{DD}$. Data are mean +/- SD, n=3 (**D**) Graph plotting the difference in H/D exchange level for each studied peptide. Values indicate the sum of differences measured at three deuteration times (3, 30 and 300 sec), as the product of differences in % deuteration (%D) * the number of deuterons (#D).

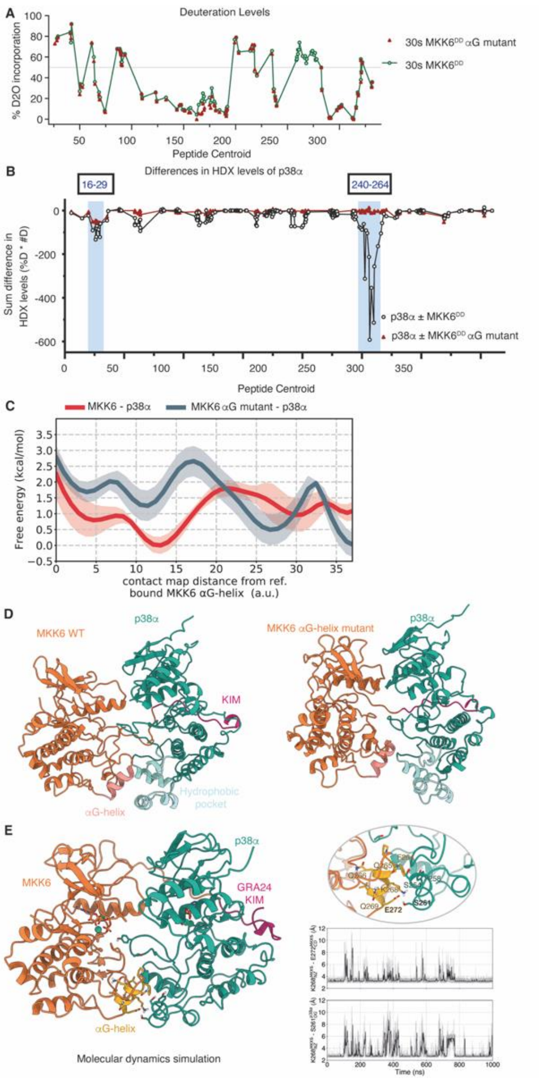

**Fig. S9. The MKK6 αG-helix – p38α hydrophobic pocket interaction is stable and the MKK6$^{DD}$ αG-helix mutant abolishes the interaction.** (**A**) Deuteration levels for each peptide of both MKK6$^{DD}$ and MKK6$^{DD}$ αG-helix mutant. Each dot represents one peptide plotted on the x-axis according to the central residue of the peptide (centroid). (**B**) Two regions of p38α are protected from exchange upon MKK6$^{DD}$ binding: residues 16-29 and residues 240-264, with the 240-264 region showing higher protection levels compared to the N-terminal region. Only the 16-29 region of p38α is protected from exchange upon MKK6$^{DD}$αG-helix mutant binding. (**C**) p38α-MKK6 (red) and p38α-MKK6 αG-helix mutant (blue) free energy profiles as a function of the distance to the native contact map of the cryo-EM structure at the C-lobe interface. Shaded error bands show the estimates of uncertainty in the free energy in each region of the CV space. (**D**) Representative structures of p38α-MKK6 (left) and p38α-MKK6 αG-helix mutant (right) found in the free energy global minima are shown in cartoon representation. The C-to-C-lobe interface is maintained in p38α-MKK6. Conversely, the p38α-MKK6 αG-helix mutant populates conformations showing the detachment of MKK6$^{DD}$ αG-helix from the p38α hydrophobic pocket. (**E**) Important interactions around the hydrophobic patch maintained over the course of the MD simulations, inset shows details of observed interactions and plots of distances during the simulation.

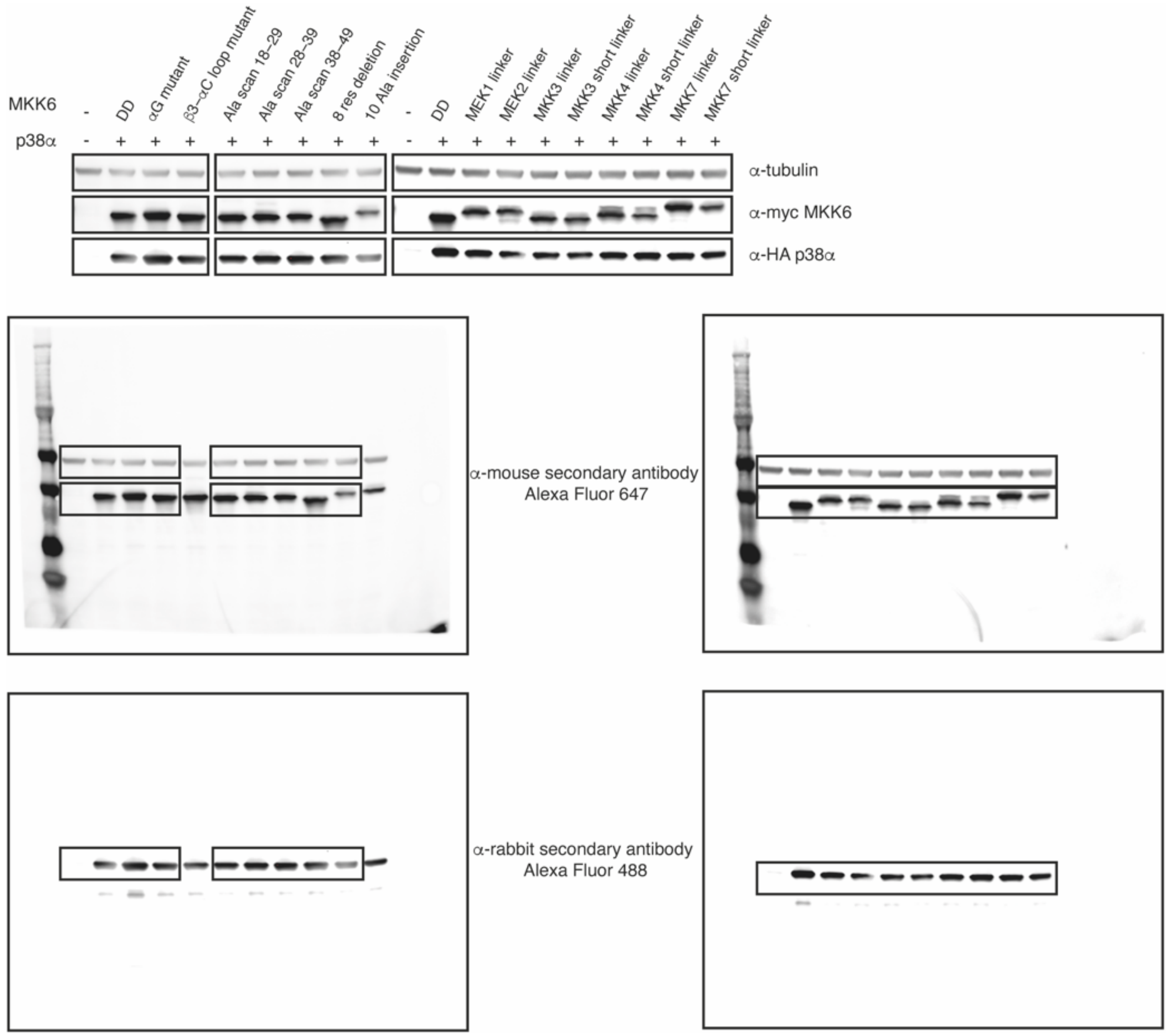

**Fig. S10. Expression levels of p38α and MKK6 mutants used in cellular assays.** Western blots of total protein extracts from co-transfected HEK293-T cells. Uncropped blots are shown below.

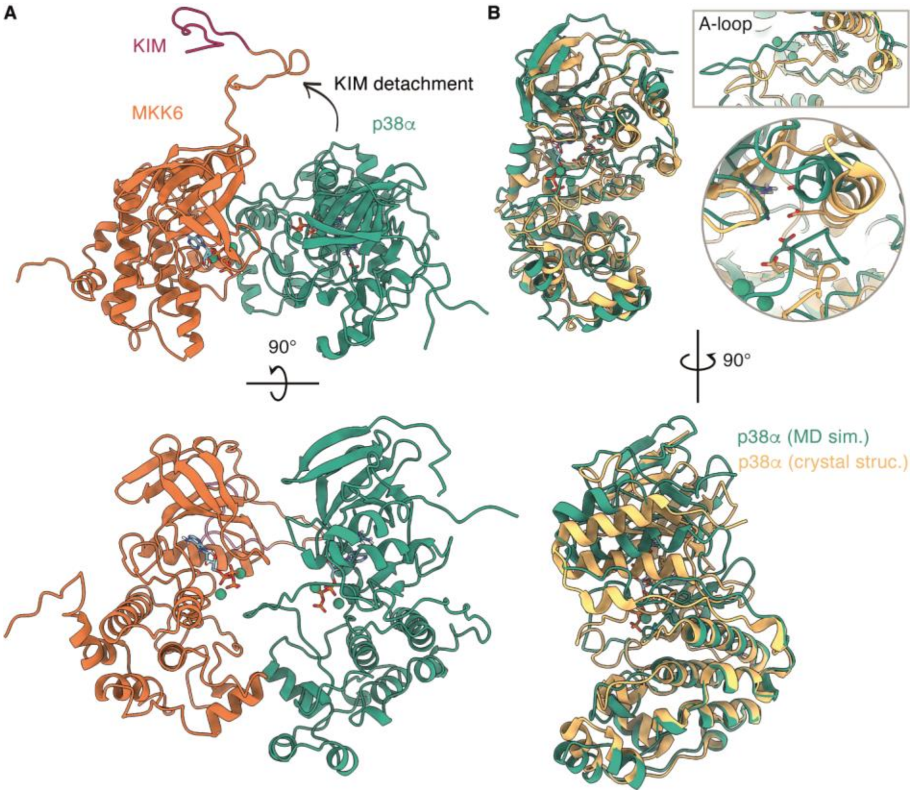

**Fig. S11. Communication between the MKK6 KIM and p38α.** (**A**) Top and side views of the complex after the detachment of the KIM and consequent transition of p38α to an inactive-like conformation. (**B**) Superposition of p38α with the inactive p38α crystal structure (PDB 3s3i), $RMSD_{backbone}^{p38\alpha}$ = 3.5 Å. Detail: *Top:* A-loop that breaks the β-sheet motif normally seen in the active conformation and adopts an inactive-like conformation, *Bottom:* αC-helix and DFG motif and K/R53-E71 salt-bridge.

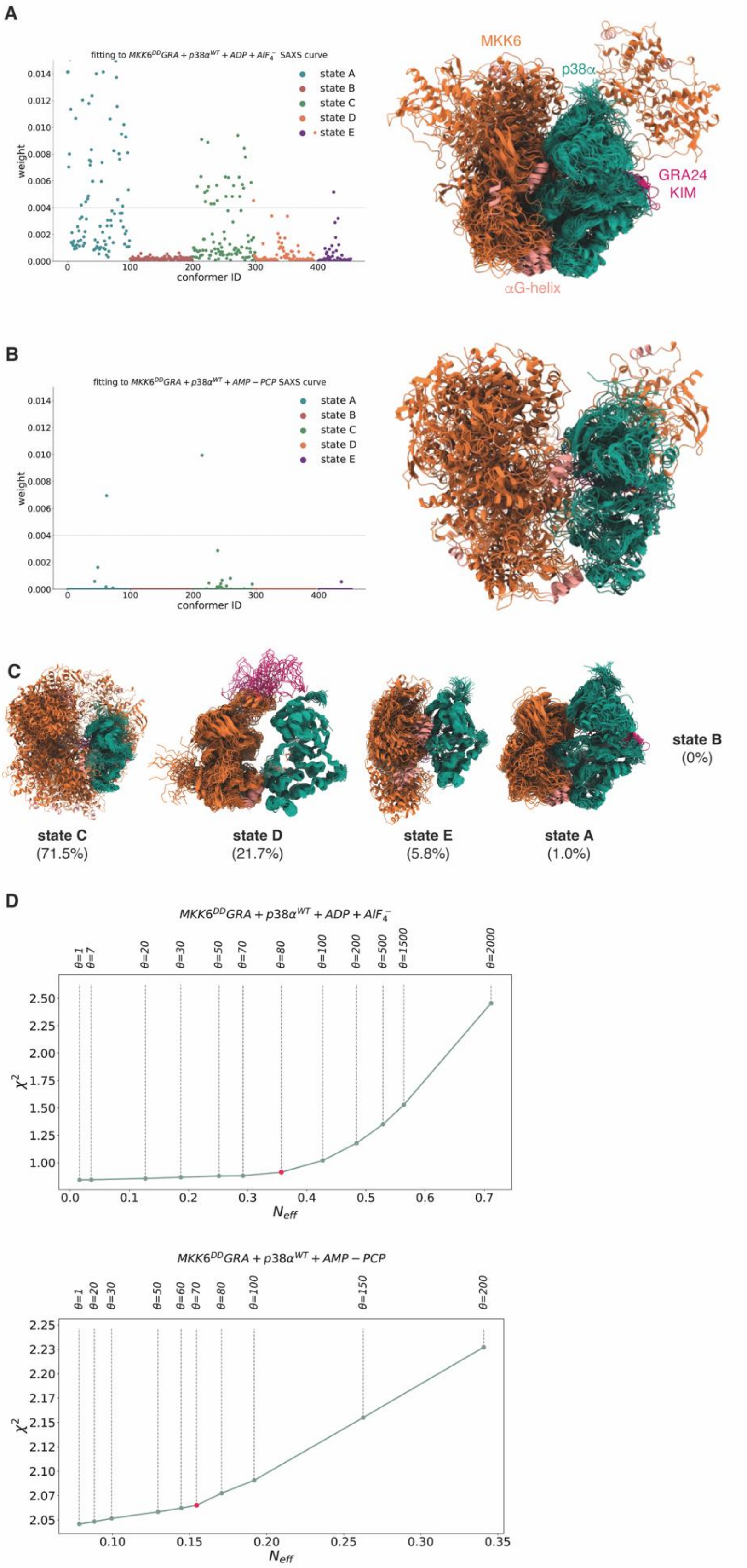
A
fitting to $MKK6^{DD}GRA + p38\alpha^{WT} + ADP + AlF_4^-$ SAXS curve
state A
state B
state C
state D
state E
weight
conformer ID
MKK6
p38α
GRA24
KIM
αG-helix
B
fitting to $MKK6^{DD}GRA + p38\alpha^{WT} + AMP-PCP$ SAXS curve
state A
state B
state C
state D
state E
weight
conformer ID
C
state C
(71.5%)
state D
(21.7%)
state E
(5.8%)
state A
(1.0%)
state B
(0%)
D
$MKK6^{DD}GRA + p38\alpha^{WT} + ADP + AlF_4^-$
θ=1
θ=7
θ=20
θ=30
θ=50
θ=70
θ=80
θ=100
θ=200
θ=500
θ=1500
θ=2000
$\chi^2$
$N_{eff}$
$MKK6^{DD}GRA + p38\alpha^{WT} + AMP-PCP$
θ=1
θ=20
θ=30
θ=50
θ=60
θ=70
θ=80
θ=100
θ=150
θ=200
$\chi^2$
$N_{eff}$

**Fig. S12. SAXS-based refinement of the MD-derived conformational ensemble through Bayesian/maximum entropy.** (**A**) Statistical weights of the conformers after fitting ($\chi^2$=0.89) to the MKK6$^{DD}$GRA + p38α$^{WT}$ + ADP + $AlF_4^-$ SAXS curve (Fig. S2). Graphical representation of the conformations with a weight higher than 0.004. (**B**) Statistical weights of the conformers after fitting ($\chi^2$=2.1) to the MKK6$^{DD}$GRA + p38α$^{WT}$ + AMP-PCP SAXS curve (Fig. S2). Graphical representation of the conformations with a weight higher than 0.004. (**C**) Population of states as derived from the fitting to the MKK6$^{DD}$GRA + p38α$^{WT}$ + AMP-PCP SAXS curve. (**D**) Scan of θ values used in reweighting ensembles against SAXS data with the iBME approach. For each ensemble, the θ corresponding to the red marker was chosen to reweight the ensemble. At this θ, we find a refined ensemble that minimizes the $\chi^2$ between the calculated and experimental scattering intensities, while retaining a significant fraction of frames in the posterior distribution.

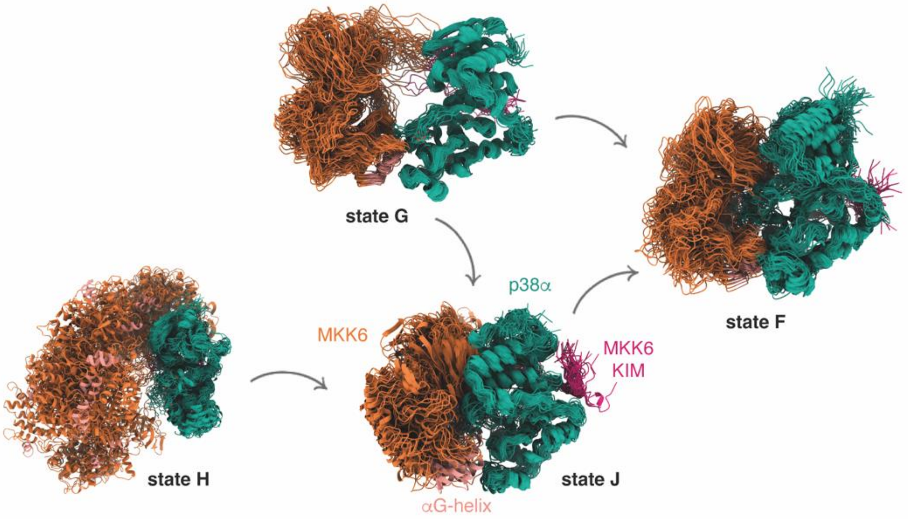

**Fig. S13. Kinetic-based clustering of the accumulated simulations of MKK6-p38α.** Each macro-state shows an overlay of 50 representative conformations sampled proportionally to the equilibrium probability of each microstate in the corresponding macro-state and correspond to different kinetically distinct states.

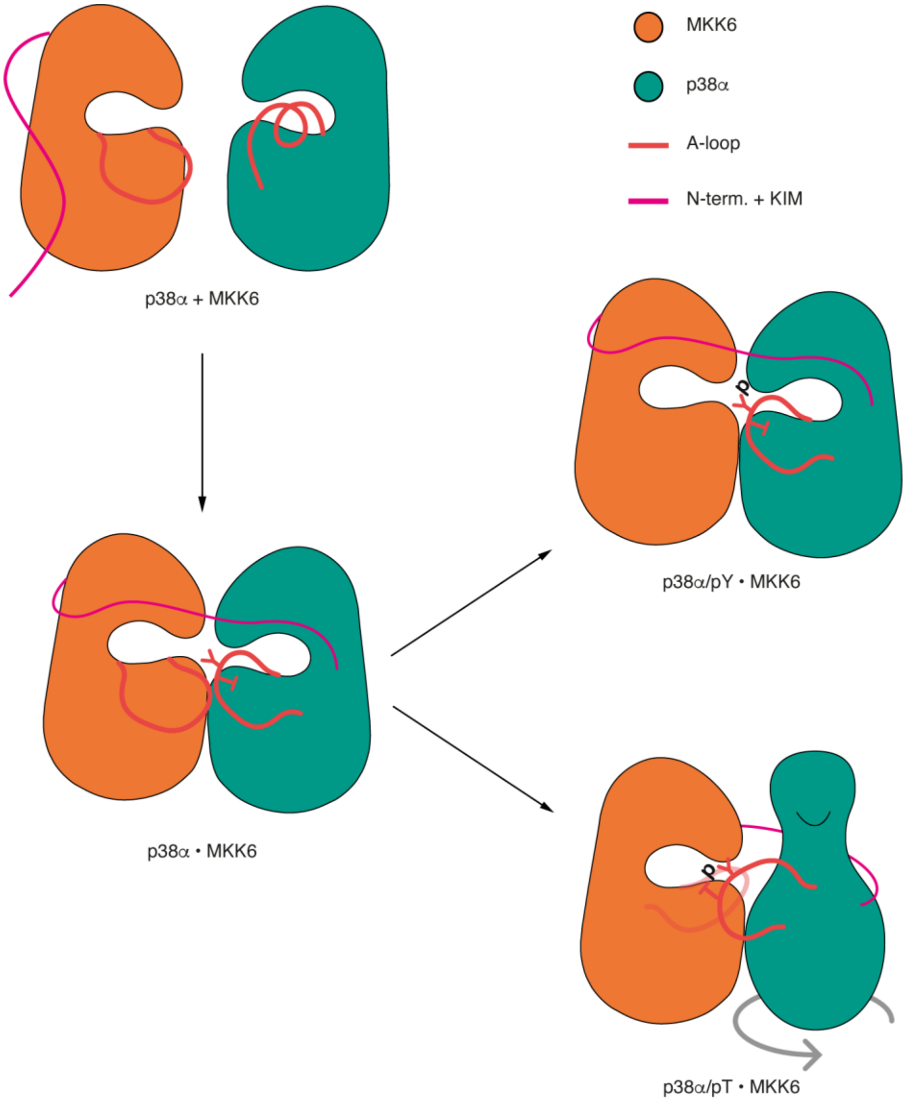

**Fig. S14. Schematic representation of the phosphorylation mechanism derived from the MD simulations.** Although both p38α T180 and Y182 can reach MKK6 ATP at a catalytically competent distance, the N-lobe of p38α seems to have to rotate for T180 to reach MKK6 ATP in most replicas. The difference in experimentally derived kinetic rates measured for the first phosphorylation step may reflect the rotation of the N-lobe of p38α around its axis, which seems to be associated only with the T180 phosphorylation.

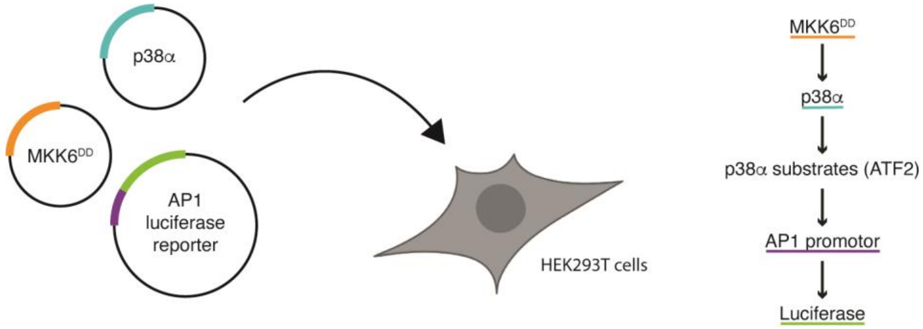

**Fig. S15. Cellular reporter assay.** HEK293T cells are transiently transfected with MKK6$^{DD}$ mutants (orange) and p38α (teal), together with a plasmid encoding firefly luciferase (green) under the control of the AP-1 promoter (purple). When p38α is activated, it phosphorylates several substrates, including ATF2, that will in turn stimulate the AP-1 promoter and trigger the expression of luciferase. Activity of p38α can be directly monitored by measurement of luminescence.

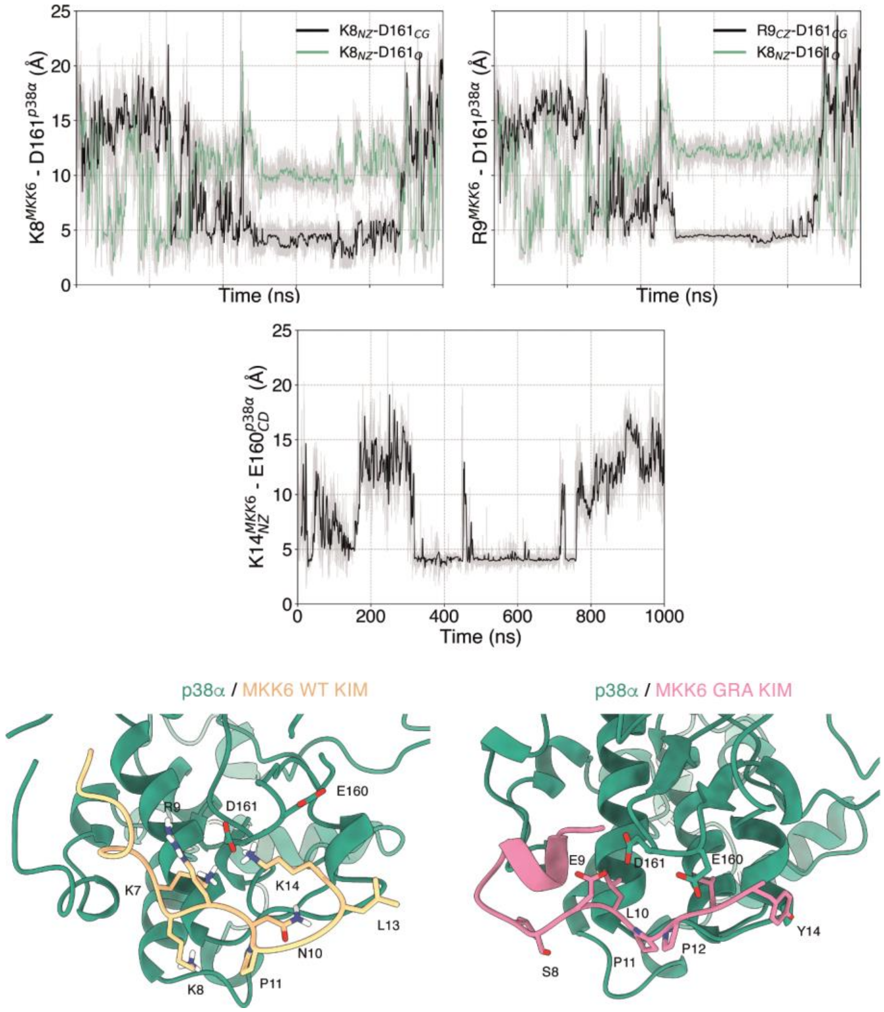

**Fig. S16. Important interactions that maintain the KIM of MKK6 in contact with p38α over the course of the MD simulations.** The rolling average of the timeseries of side-chain-to-side-chain interactions is shown in black, while the side-chain-to-backbone interactions are shown in green. The reported timeseries refer to one of the simulations with the MKK6 WT sequence (Table S6). However, the same pattern of interactions is observed in three out of the five independent replicas where p38α stays in contact with MKK6.

**Table S1. Calculated SAXS data using Scatter and FoxS.**

| | I(0) | Rg (Å) | MW estimation (kDa) | $D_{max}$ (Å) | $\chi^2$ against cryo-EM MKK6$^{DD}$GRA + p38α$^{T180V}$ model | $\chi^2$ against MD MKK6 + rotated p38α$^{WT}$ model |
|---|---|---|---|---|---|---|
| **MKK6$^{DD}$GRA + p38α$^{WT}$ + AMP-PCP** | 0.30 | 41.6 | 68 | 139 | 136 | 94.0 |
| **MKK6$^{DD}$GRA + p38α$^{T180V}$ + AMP-PCP** | 0.23 | 39.1 | 77 | 140 | 138 | 96.6 |
| **MKK6$^{DD}$GRA + p38α$^{Y182F}$ + AMP-PCP** | 0.30 | 39.4 | 70 | 139 | 165 | 115 |
| **MKK6$^{DD}$GRA + p38α$^{WT}$ + ADP + $AlF_4^-$** | 0.26 | 32.2 | 65 | 121 | 19.1 | 10.1 |
| **MKK6$^{DD}$GRA + p38α$^{T180V}$ + ADP + $AlF_4^-$** | 0.23 | 29.6 | 59 | 115 | 5.91 | 6.46 |
| **MKK6$^{DD}$GRA + p38α$^{Y182F}$ + ADP + $AlF_4^-$** | 0.28 | 35.3 | 69 | 134 | 86.6 | 55.1 |
| **cryo-EM MKK6$^{DD}$GRA + p38α$^{T180V}$ model** | | 29* | | | | |
| **MD MKK6 + rotated p38α$^{WT}$ model** | | 32* | | | | |

* Theoretical Rg calculated using ATSAS

**Table S2. X-ray data processing and refinement statistics.**

| Structure | p38α (PDB-5ETC) | p38α$^{K53R}$ (PDB-5ETI) |
|---|---|---|
| Space group | $P2_12_12_1$ | $P2_12_12_1$ |
| Wavelength | 0.873 Å | 1.063 Å |
| Unit cell dimensions (Å) a, b, c | 45.1, 86.9, 124.0 | 45.4, 87.0, 122.9 |
| α, β, γ (°) | 90.0, 90.0, 90.0 | 90.0, 90.0, 90.0 |
| Resolution range (Å) | 20-2.42 | 20-2.8 |
| Number of unique reflections | 16774 | 10748 |
| Multiplicity[1] | 3.7 (2.8) | 3.9 (3.9) |
| Completeness[1] (%) | 87.3 (52.3) | 87.9 (90.8) |
| Rmerge[1] | 0.09 (0.50) | 0.17 (0.58) |
| <I/ σ(I)>[1] | 11.0 (1.9) | 8.3 (3.1) |
| Wilson B factor | 26 Å$^2$ | 28 Å$^2$ |
| No. of atoms | 3062 | 2918 |
| Protein | 2865 | 2867 |
| Ligands/ion | 5 | 0 |
| Water | 192 | 64 |
| R-factor[3] (%) | 19.4 | 17.8 |
| Free R-factor[4] (%) | 24.2 | 22.5 |
| RMS deviations: | | |
| Bonds (Å) | 0.013 | 0.008 |
| Angles (°) | 1.37 | 1.23 |

[1] Statistics for the highest resolution bin (2.95-2.8; 2.52-2.4) are shown in parenthesis

**Table S3. Summary of cross-correlation scores for the rebuilt model and the predicted structures for different regions of each protein.** The highest cross-correlation score is highlighted. The region with the highest cross-correlation score from each model was used in the final model.

| | **Entire complex** | **MKK6-p38α hydrophobic patch**[1] | **MKK6 KIM domain**[2] | **p38α A-loop**[3] | **MKK6 region close to the linker**[4] |
|---|---|---|---|---|---|
| Rebuilt model | 0.492 | 0.441 | 0.488 | 0.305 | 0.248 |
| AF2 model1 | 0.271 | 0.152 | 0.349 | 0.288 | 0.272 |
| AF2 model2 | 0.204 | 0.190 | 0.401 | 0.232 | 0.010 |
| MODELLER model1 | 0.477 | 0.497 | 0.450 | 0.307 | 0.239 |
| MODELLER model2 | 0.474 | 0.486 | 0.427 | 0.317 | 0.226 |
| MODELLER model3 | 0.462 | 0.478 | 0.436 | 0.320 | 0.140 |
| MODELLER model4 | 0.486 | 0.498 | 0.439 | 0.322 | 0.263 |
| MODELLER model5 | 0.479 | 0.396 | - | 0.315 | - |
| Conformation derived from MD simulations clustering | 0.283 | 0.242 | 0.351 | 0.261 | 0.174 |

[1] MKK6: res. 262-275, p38α: res. 252-262

[2] MKK6: res. 0-15, p38α: res. 108-136, 156-167, 309-318

[3] p38α: res. 172-189

[4] MKK6: res. 36-48

## Table S4. Cryo-EM data collection, processing and refinement.

| **Data collection and processing** | **MKK6$^{DD}$GRA-p38α$^{T180V}$ complex (PDB-8A8M) (EMDB-15233)** |
|---|---|
| Microscope | Titan Krios |
| Camera | K2 |
| Voltage (kV) | 300 |
| Camera Magnification | 215,000 |
| Pixel size (Å) | 0.638 |
| Electron exposure ($e^-$/Å$^2$) | 62.77 |
| Exposure rate ($e^-$/pixel/sec) | 12.8 |
| Number of frames per exposure | 40 |
| Defocus range (µm) | -1.5 to -3 |
| Automation software | SerialEM |
| Micrographs collected (no.) | 28,633 |
| Micrographs used (no.) | 26,017 |
| Total extracted particles (no.) | 2,825,821 |
| Refined particles (no.) | 86,510 |
| Final particle images (no.) | 35,123 |
| Map resolution (Å) | 4.0 |
| FSC 0.5 (Å unmasked/masked) | 8.2 / 5.8 |
| FSC 0.143 (Å unmasked/masked) | 5.8 / 4.0 |
| Map resolution range (Å) | 2.7-6.5 |
| Map resolution range due to anisotropy (Å) | |
| Map sharpening B factor (Å$^2$) | 200 |
| Map sharpening method | cryoSPARC |
| **Model Composition** | |
| Initial models used | 5ETA, 5ETC and a homology model of 6YG1 |
| Non-hydrogen atoms | 5249 |
| Protein residues | 5157 |
| Ligands | 92 |
| **Refinement** | |
| Refinement package | Phenix |
| Real or reciprocal space | Real |
| Resolution cutoff (Å) | 4.0 |
| Model-Map scores | |
| CC | 0.78 |
| FSC 0.5 (Å) | 8.1 |
| B factors (Å$^2$) | |
| Protein | 182.4 |
| Ligands | - |
| R.M.S deviations | |
| Bond length (Å) | 0.004 |
| Bond angles (°) | 0.934 |
| Validation | |
| MolProbity score | 2.44 |
| CaBLAM outliers | 3.96 |
| Clash score | 28.69 |
| Poor rotamers (%) | 0.52 |
| Ramachandran plot | |
| Favoured (%) | 91.69 |
| Allowed (%) | 8.31 |
| Outliers (%) | 0 |

**Table S5. HDX results**
Provided in .xlsx file format

**Table S6. Statistical analysis of cellular assay (Fig. 2).**

| p38α | MKK6 | Mean | se | Shapiro Wilk | Welch t test against p38α+/MKK6$^{DD}$ | Significance (<0.5 *; <0.01 **; < 0.001 ***) | MKK6 mutant:p38α expression ratio (sd in parentheses)[1] |
|---|---|---|---|---|---|---|---|
| + | - | 2% | 0.002 | 0.436 | 3.66E-12 | *** | |
| + | DD[2] | 100 % | 0.057 | 0.771 | 1.00E+00 | NS | 100 % |
| + | αG-helix mutant[3] | 31 % | 0.023 | 0.776 | 1.68E-10 | *** | 89 % (7 %) |
| + | β3-αC-loop mutant[4] | 168 % | 0.122 | 0.821 | 3.57E-04 | *** | 113 % (12 %) |

[1] The expression of the proteins was quantified by western blotting (Fig. S10) and normalized against the MKK6$^{DD}$:p38α pair (the reported value is the average ratio of triplicates)

[2] S207D, T211D

[3] F264A, Q265A, L267A, K268A, E272A

[4] T87A, V88A, N89A

**Table S7. Summary of the unbiased simulations of the MKK6-p38α.** The reported times correspond to the simulation time of each independent unbiased simulation. In the case of the adaptive sampling simulations, we report the accumulated simulation time of all epochs.

* started from a conformation originating from the restrained simulations of MKK6GRA-p38α, where p38α Y182 was close to MKK6 ATP.

| **System** | | **Simulation time (ns)** | **Inter-kinase contacts restraints** |
|---|---|---|---|
| p38α-MKK6GRA | rep1 | 1000 | No |
| | rep2 | 1000 | No |
| | rep3 | 1000 | No |
| | rep4 | 1000 | No |
| | rep5 | 1000 | No |
| | adaptive sampling | 9200 | No |
| p38α-MKK6GRA | rep1 | 1000 | Yes |
| | rep2 | 1000 | Yes |
| | rep3 | 1000 | Yes |
| | rep4 | 1000 | Yes |
| | rep5 | 1000 | Yes |
| p38α-MKK6GRA | rep1 | 1000 | No* |
| | rep2 | 1000 | No* |
| | rep3 | 2000 | No* |
| p38α-MKK6 WT | rep1 | 1000 | No |
| | rep2 | 1000 | No |
| | rep3 | 1000 | No |
| | rep4 | 1000 | No |
| | rep5 | 1000 | No |
| | adaptive sampling | 9600 | No |
| **Total simulation time** | | 37800 | |

**Table S8. Comparison of MD-derived atom distances (Å) important for the phosphorylation of p38α at T180 and Y182 by MKK6 with atom distances reported for the SP20 phosphoryl transfer mechanism catalysed by the cAMP-dependent protein kinase (PKA).** The reported distances for the PKA-SP20 phosphorylation were derived from QM/MM calculations *(47)*, while the MD distances where derived from a frame where either T180 or Y182 was the closest to MKK6 ATP.

| | QM/MM | MD simulations | | | |
|---|---|---|---|---|---|
| | **PKA-SP20** | **MKK6GRA-p38α** (rep3 / rep5, no restraints) | **MKK6GRA-p38α** (rep3 / rep4, with restraints) | **MKK6GRA-p38α** (rep3, released restraints) | **MKK6-p38α** (rep2 / rep5, no restraints) |
| ATP$_{(P\gamma)}$-T180$_{(OH)}$ | 3.76 | 3.3 / 16.5 | 10.4 / 14.4 | 13.0 | 13.5 / 5.6 |
| T180$_{(HG1)}$-ATP$_{(OG1)}$ | 1.81 | 1.6 / 15.2 | 11.3 / 13.3 | 14.0 | 17.8 / 8.7 |
| T180$_{(HG1)}$-ATP$_{(OG2)}$ | | 2.9 / 17.5 | 9.1 / 14.8 | 15.2 | 15.2 / 8.1 |
| T180$_{(HG1)}$-ATP$_{(OG3)}$ | | 1.7 / 16.1 | 9.6 / 15.8 | 12.8 | 17.0 / 7.8 |
| ATP$_{(P\gamma)}$-Y182$_{(OH)}$ | 3.76 | 17.4 / 3.8 | 4.4 / 3.5 | 3.6 | 4.3 /15.1 |
| Y182$_{(HH)}$-ATP$_{(OG1)}$ | 1.81 | 17.3 / 1.9 | 5.0 / 1.4 | 3.7 | 7.3 / 19.1 |
| Y180$_{(HH)}$-ATP$_{(OG2)}$ | | 17.5 / 3.8 | 3.3 / 3.6 | 4.8 | 7.5/ 18.3 |
| Y182$_{(HH)}$-ATP$_{(OG3)}$ | | 16.9 / 3.7 | 2.9 / 3.9 | 2.6 | 7.5 / 17.9 |

**Table S9. Statistical analysis of cellular assay (Fig. 5).**

| **p38α** | **MKK6** | **Mean** | **se** | **Shapiro Wilk** | **Welch t-test against p38α+ /MKK6$^{DD}$** | **Wilcoxon rank sum exact test against p38α+ /MKK6$^{DD}$** | **Significance (<0.5 *; <0.01 **; < 0.001 ***)** | **MKK6 mutant:p38α expression ratio (sd in parentheses)[1]** |
|---|---|---|---|---|---|---|---|---|
| + | - | 2 % | 0.004 | 2.47E-01 | 1.43E-11 | | *** | |
| + | DD | 100 % | 0.055 | 1.32E-01 | 1.00E+00 | | NS | 100 % |
| + | Ala scan 18-29 | 73 % | 0.054 | 4.37E-01 | 2.09E-03 | | ** | 116 % (10 %) |
| + | Ala scan 28-39 | 101 % | 0.078 | 2.32E-01 | 8.84E-01 | | NS | 83 % (12 %) |
| + | Ala scan 38-49 | 42 % | 0.022 | 4.35E-01 | 6.15E-09 | | *** | 81 % (18 %) |
| + | MEK1 linker | 12 % | 0.007 | 9.16E-01 | 5.63E-11 | | *** | 80 % (11 %) |
| + | MEK2 linker | 14 % | 0.017 | 1.01E-01 | 1.72E-11 | | *** | 89 % (18 %) |
| + | MKK3 linker | 44 % | 0.028 | 6.96E-01 | 9.74E-09 | | *** | 100 % (29 %) |
| + | MKK3 short linker | 44 % | 0.035 | 5.61E-02 | 9.76E-09 | | *** | 89 % (13 %) |
| + | MKK4 linker | 29 % | 0.045 | 1.83E-02 | | 1.96E-06 | *** | 88 % (17 %) |
| + | MKK4 short linker | 16 % | 0.017 | 4.83E-01 | 2.11E-11 | | *** | 60 % (8 %) |
| + | MKK7 linker | 34 % | 0.029 | 2.54E-01 | 5.77E-10 | | *** | 89 % (12 %) |
| + | MKK7 short linker | 26 % | 0.037 | 4.95E-01 | 6.70E-11 | | *** | 70 % (19 %) |
| + | 8 res deletion | 50 % | 0.040 | 1.37E-01 | 1.22E-07 | | *** | 112 % (5 %) |
| + | 10 Ala insertion | 53 % | 0.040 | 3.87E-01 | 3.47E-07 | | *** | 80 % (17 %) |

[1] The expression of the proteins was quantified by western blotting (Fig. S10) and normalized against the MKK6$^{DD}$:p38α pair (the reported value is the average ratio of triplicates)

**Table S10. SAXS data collection and analysis**

| **Data-collection parameters** | |
|---|---|
| Instrument: | Diamond light source B21 |
| Wavelength (Å) | 0.9524 |
| q-range (Å$^{-1}$) | 0.0026-0.34 |
| Sample-to-detector distance (m) | 3.7 |
| Concentration (mg/mL) | 5 |
| Temperature (K) | 277 |
| Detector | Eiger 4M (Dectris) |
| Flux (photons/s) | $2*10^{12}$ |
| Beam size (µm) | 1102*240 |

| **Structural parameters (AMP-PCP)** | **MKK6$^{DD}$GRA + p38$\alpha^{WT}$ + AMP-PCP** | **MKK6$^{DD}$GRA + p38$\alpha^{T180V}$ + AMP-PCP** | **MKK6$^{DD}$GRA + p38$\alpha^{Y182F}$ + AMP-PCP** |
|---|---|---|---|
| I0 (kDa) [from Guinier] | 3.00E-01 | 2.30E-01 | 3.00E-01 |
| Rg (Å) [from Guinier] | 41.6 | 39.1 | 39.4 |
| qminRg – qmaxRg used for Guinier | $1.4*10^{-2}$-$3.1*10^{-2}$ | $1.8*10^{-2}$-$3.3*10^{-2}$ | $1.6*10^{-2}$-$3.2*10^{-2}$ |
| Volume (Å$^3$) | $1.5*10^5$ | $1.5*10^5$ | $1.4*10^5$ |
| D$_{max}$ (Å) | 139 | 140 | 139 |
| Calculated MW | 68 | 77 | 70 |

| **Structural parameters (ADP + AlF$_4^-$)** | **MKK6$^{DD}$GRA + p38$\alpha^{WT}$ + ADP + AlF$_4^-$** | **MKK6$^{DD}$GRA + p38$\alpha^{T180V}$ + ADP + AlF$_4^-$** | **MKK6$^{DD}$GRA + p38$\alpha^{Y182F}$ + ADP + AlF$_4^-$** |
|---|---|---|---|
| I0 (kDa) [from Guinier] | 2.60E-01 | 2.30E-01 | 2.80E-01 |
| Rg (Å) [from Guinier] | 32.2 | 29.6 | 35.3 |
| qminRg – qmaxRg used for Guinier | $1.4*10^{-2}$-$4.0*10^{-2}$ | $1.7*10^{-2}$-$4.3*10^{-2}$ | $1.4*10^{-2}$-$3.6*10^{-2}$ |
| Volume (Å$^3$) | $1.3*10^5$ | $1.2*10^5$ | $1.4*10^5$ |
| D$_{max}$ (Å) | 121 | 115 | 134 |
| Calculated MW | 65 | 59 | 69 |

| **Software employed** | |
|---|---|
| Primary data reduction: | B21 autoprocessing pipeline |
| Data processing | Scatter IV |
| $\chi^2$ determination | FoXs |

**Movie S1.** Detailed presentation of the fitting of the MKK6$^{DD}$GRA-p38α$^{T180V}$ model in the cryo-EM map and general overview of the model.

**Movie S2.** Close-up view of the interaction between the αG-helices of p38α and MKK6 in the sharpened Coulomb potential map (black mesh).

**Movie S3.** Simple morph between inactive p38α with an occluded A-loop conformation to the MKK6 engaged conformation.

**Movie S4**. MD simulation trajectory (1 µs long, unrestrained) where the N-lobe of p38α rotates to allow access of T180 to the ATP bound to MKK6.

**Movie S5.** MD simulation trajectory (1 µs long, unrestrained) where Y182 approaches the γ-phosphate of ATP bound to MKK6.

**Movies S6-S10.** Overview of the ensemble of conformations corresponding to the macro-states that represent the whole set of the MD simulations of the MKK6GRA-p38α$^{WT}$. ATP, T180 and Y182 are shown in stick representation.

**Movies S11-S14.** Overview of the ensemble of conformations corresponding to the macro-states that represent the whole set of the MD simulations of the MKK6-p38α$^{WT}$. ATP, T180 and Y182 are shown in stick representation.

**Movie S15.** Overview of the ensemble of conformations that best describes the MKK6$^{DD}$GRA + p38α$^{WT}$ + ADP + $AlF_4^-$ SAXS curves (Fig. S2) as derived from the Bayesian/maxim entropy framework for ensemble refinement we applied on the MD-derived structures.

**Movie S16.** Overview of the ensemble of conformations that best describes the MKK6$^{DD}$GRA + p38α$^{WT}$ + AMP-PCP SAXS curves (Fig. S2) as derived from the Bayesian/maxim entropy framework for ensemble refinement we applied on the MD-derived structures.

## References and Notes

1. B. Canovas, A. R. Nebreda, Diversity and versatility of p38 kinase signalling in health and disease. *Nat. Rev. Mol. Cell Biol.* **22**, 346–366 (2021). doi:10.1038/s41580-020-00322-w Medline

2. M. Bouhaddou, D. Memon, B. Meyer, K. M. White, V. V. Rezelj, M. Correa Marrero, B. J. Polacco, J. E. Melnyk, S. Ulferts, R. M. Kaake, J. Batra, A. L. Richards, E. Stevenson, D. E. Gordon, A. Rojc, K. Obernier, J. M. Fabius, M. Soucheray, L. Miorin, E. Moreno, C. Koh, Q. D. Tran, A. Hardy, R. Robinot, T. Vallet, B. E. Nilsson-Payant, C. Hernandez-Armenta, A. Dunham, S. Weigang, J. Knerr, M. Modak, D. Quintero, Y. Zhou, A. Dugourd, A. Valdeolivas, T. Patil, Q. Li, R. Hüttenhain, M. Cakir, M. Muralidharan, M. Kim, G. Jang, B. Tutuncuoglu, J. Hiatt, J. Z. Guo, J. Xu, S. Bouhaddou, C. J. P. Mathy, A. Gaulton, E. J. Manners, E. Félix, Y. Shi, M. Goff, J. K. Lim, T. McBride, M. C. O’Neal, Y. Cai, J. C. J. Chang, D. J. Broadhurst, S. Klippsten, E. De Wit, A. R. Leach, T. Kortemme, B. Shoichet, M. Ott, J. Saez-Rodriguez, B. R. tenOever, R. D. Mullins, E. R. Fischer, G. Kochs, R. Grosse, A. García-Sastre, M. Vignuzzi, J. R. Johnson, K. M. Shokat, D. L. Swaney, P. Beltrao, N. J. Krogan, The Global Phosphorylation Landscape of SARS-CoV-2 Infection. *Cell* **182**, 685–712.e19 (2020). doi:10.1016/j.cell.2020.06.034 Medline

3. D. S. Battagello, G. Dragunas, M. O. Klein, A. L. P. Ayub, F. J. Velloso, R. G. Correa, Unpuzzling COVID-19: Tissue-related signaling pathways associated with SARS-CoV-2 infection and transmission. *Clin. Sci.* **134**, 2137–2160 (2020). doi:10.1042/CS20200904 Medline

4. S. Bellon, M. J. Fitzgibbon, T. Fox, H.-M. Hsiao, K. P. Wilson, The structure of phosphorylated p38γ is monomeric and reveals a conserved activation-loop conformation. *Structure* **7**, 1057–1065 (1999). doi:10.1016/S0969-2126(99)80173-7 Medline

5. S. S. Taylor, A. P. Kornev, Protein kinases: Evolution of dynamic regulatory proteins. *Trends Biochem. Sci.* **36**, 65–77 (2011). doi:10.1016/j.tibs.2010.09.006 Medline

6. N. Blüthgen, F. J. Bruggeman, S. Legewie, H. Herzel, H. V. Westerhoff, B. N. Kholodenko, Effects of sequestration on signal transduction cascades. *FEBS J.* **273**, 895–906 (2006). doi:10.1111/j.1742-4658.2006.05105.x Medline

7. F. Ortega, L. Acerenza, H. V. Westerhoff, F. Mas, M. Cascante, Product dependence and bifunctionality compromise the ultrasensitivity of signal transduction cascades. *Proc. Natl. Acad. Sci. U.S.A.* **99**, 1170–1175 (2002). doi:10.1073/pnas.022267399 Medline

8. M. Thattai, A. van Oudenaarden, Attenuation of noise in ultrasensitive signaling cascades. *Biophys. J.* **82**, 2943–2950 (2002). doi:10.1016/S0006-3495(02)75635-X Medline

9. D. Hammaker, G. S. Firestein, “Go upstream, young man”: Lessons learned from the p38 saga. *Ann. Rheum. Dis.* **69**, i77–i82 (2010). doi:10.1136/ard.2009.119479 Medline

10. K. P. Wilson, M. J. Fitzgibbon, P. R. Caron, J. P. Griffith, W. Chen, P. G. McCaffrey, S. P. Chambers, M. S.-S. Su, Crystal structure of p38 mitogen-activated protein kinase. *J. Biol. Chem.* **271**, 27696–27700 (1996). doi:10.1074/jbc.271.44.27696 Medline

11. X. Xie, Y. Gu, T. Fox, J. T. Coll, M. A. Fleming, W. Markland, P. R. Caron, K. P. Wilson, M. S.-S. Su, Crystal structure of JNK3: A kinase implicated in neuronal apoptosis. *Structure* **6**, 983–991 (1998). doi:10.1016/S0969-2126(98)00100-2 Medline

12. F. Zhang, A. Strand, D. Robbins, M. H. Cobb, E. J. Goldsmith, Atomic structure of the MAP kinase ERK2 at 2.3 A resolution. *Nature* **367**, 704–711 (1994). doi:10.1038/367704a0 Medline

13. X. Min, R. Akella, H. He, J. M. Humphreys, S. E. Tsutakawa, S.-J. Lee, J. A. Tainer, M. H. Cobb, E. J. Goldsmith, The structure of the MAP2K MEK6 reveals an autoinhibitory dimer. *Structure* **17**, 96–104 (2009). doi:10.1016/j.str.2008.11.007 Medline

14. T. Matsumoto, T. Kinoshita, H. Matsuzaka, R. Nakai, Y. Kirii, K. Yokota, T. Tada, Crystal structure of non-phosphorylated MAP2K6 in a putative auto-inhibition state. *J. Biochem.* **151**, 541–549 (2012). doi:10.1093/jb/mvs023 Medline

15. J. F. Ohren, H. Chen, A. Pavlovsky, C. Whitehead, E. Zhang, P. Kuffa, C. Yan, P. McConnell, C. Spessard, C. Banotai, W. T. Mueller, A. Delaney, C. Omer, J. Sebolt-Leopold, D. T. Dudley, I. K. Leung, C. Flamme, J. Warmus, M. Kaufman, S. Barrett, H. Tecle, C. A. Hasemann, Structures of human MAP kinase kinase 1 (MEK1) and MEK2 describe novel noncompetitive kinase inhibition. *Nat. Struct. Mol. Biol.* **11**, 1192–1197 (2004). doi:10.1038/nsmb859 Medline

16. M. Schröder, L. Tan, J. Wang, Y. Liang, N. S. Gray, S. Knapp, A. Chaikuad, Catalytic Domain Plasticity of MKK7 Reveals Structural Mechanisms of Allosteric Activation and Diverse Targeting Opportunities. *Cell Chem. Biol.* **27**, 1285–1295.e4 (2020). doi:10.1016/j.chembiol.2020.07.014 Medline

17. Á. Garai, A. Zeke, G. Gógl, I. Törő, F. Fördős, H. Blankenburg, T. Bárkai, J. Varga, A. Alexa, D. Emig, M. Albrecht, A. Reményi, Specificity of linear motifs that bind to a common mitogen-activated protein kinase docking groove. *Sci. Signal.* **5**, ra74 (2012). doi:10.1126/scisignal.2003004 Medline

18. T. Tanoue, M. Adachi, T. Moriguchi, E. Nishida, A conserved docking motif in MAP kinases common to substrates, activators and regulators. *Nat. Cell Biol.* **2**, 110–116 (2000). doi:10.1038/35000065 Medline

19. W. Peti, R. Page, Molecular basis of MAP kinase regulation. *Protein Sci.* **22**, 1698–1710 (2013). doi:10.1002/pro.2374 Medline

20. A. Zeke, T. Bastys, A. Alexa, Á. Garai, B. Mészáros, K. Kirsch, Z. Dosztányi, O. V. Kalinina, A. Reményi, Systematic discovery of linear binding motifs targeting an ancient protein interaction surface on MAP kinases. *Mol. Syst. Biol.* **11**, 837 (2015). doi:10.15252/msb.20156269 Medline

21. T. Zhou, L. Sun, J. Humphreys, E. J. Goldsmith, Docking interactions induce exposure of activation loop in the MAP kinase ERK2. *Structure* **14**, 1011–1019 (2006). doi:10.1016/j.str.2006.04.006 Medline

22. C. I. Chang, B. E. Xu, R. Akella, M. H. Cobb, E. J. Goldsmith, Crystal structures of MAP kinase p38 complexed to the docking sites on its nuclear substrate MEF2A and activator MKK3b. *Mol. Cell* **9**, 1241–1249 (2002). doi:10.1016/S1097-2765(02)00525-7 Medline

23. M. Dyla, M. Kjaergaard, Intrinsically disordered linkers control tethered kinases via effective concentration. *Proc. Natl. Acad. Sci. U.S.A.* **117**, 21413–21419 (2020). doi:10.1073/pnas.2006382117 Medline

24. J. Beenstock, N. Mooshayef, D. Engelberg, How Do Protein Kinases Take a Selfie (Autophosphorylate)? *Trends Biochem. Sci.* **41**, 938–953 (2016). doi:10.1016/j.tibs.2016.08.006 Medline

25. E. Park, S. Rawson, K. Li, B.-W. Kim, S. B. Ficarro, G. G.-D. Pino, H. Sharif, J. A. Marto, H. Jeon, M. J. Eck, Architecture of autoinhibited and active BRAF-MEK1-14-3-3 complexes. *Nature* **575**, 545–550 (2019). doi:10.1038/s41586-019-1660-y Medline

26. Y. Kondo, J. Ognjenović, S. Banerjee, D. Karandur, A. Merk, K. Kulhanek, K. Wong, J. P. Roose, S. Subramaniam, J. Kuriyan, Cryo-EM structure of a dimeric B-Raf:14-3-3 complex reveals asymmetry in the active sites of B-Raf kinases. *Science* **366**, 109–115 (2019). doi:10.1126/science.aay0543 Medline

27. D. F. Brennan, A. C. Dar, N. T. Hertz, W. C. H. Chao, A. L. Burlingame, K. M. Shokat, D. Barford, A Raf-induced allosteric transition of KSR stimulates phosphorylation of MEK. *Nature* **472**, 366–369 (2011). doi:10.1038/nature09860 Medline

28. P. Sok, G. Gógl, G. S. Kumar, A. Alexa, N. Singh, K. Kirsch, A. Sebő, L. Drahos, Z. Gáspári, W. Peti, A. Reményi, MAP Kinase-Mediated Activation of RSK1 and MK2 Substrate Kinases. *Structure* **28**, 1101–1113.e5 (2020). doi:10.1016/j.str.2020.06.007 Medline

29. E. T. Haar, P. Prabakhar, X. Liu, C. Lepre, Crystal structure of the p38 α-MAPKAP kinase 2 heterodimer. *J. Biol. Chem.* **282**, 9733–9739 (2007). doi:10.1074/jbc.M611165200 Medline

30. L. Braun, M.-P. Brenier-Pinchart, M. Yogavel, A. Curt-Varesano, R.-L. Curt-Bertini, T. Hussain, S. Kieffer-Jaquinod, Y. Coute, H. Pelloux, I. Tardieux, A. Sharma, H. Belrhali, A. Bougdour, M.-A. Hakimi, A Toxoplasma dense granule protein, GRA24, modulates the early immune response to infection by promoting a direct and sustained host p38 MAPK activation. *J. Exp. Med.* **210**, 2071–2086 (2013). doi:10.1084/jem.20130103 Medline

31. E. Pellegrini, A. Palencia, L. Braun, U. Kapp, A. Bougdour, H. Belrhali, M. W. Bowler, M.-A. Hakimi, Structural Basis for the Subversion of MAP Kinase Signaling by an Intrinsically Disordered Parasite Secreted Agonist. *Structure* **25**, 16–26 (2017). doi:10.1016/j.str.2016.10.011 Medline

32. T. Bepler, A. Morin, M. Rapp, J. Brasch, L. Shapiro, A. J. Noble, B. Berger, Positive-unlabeled convolutional neural networks for particle picking in cryo-electron micrographs. *Nat. Methods* **16**, 1153–1160 (2019). doi:10.1038/s41592-019-0575-8 Medline

33. V. Modi, R. L. Dunbrack Jr., Defining a new nomenclature for the structures of active and inactive kinases. *Proc. Natl. Acad. Sci. U.S.A.* **116**, 6818–6827 (2019). doi:10.1073/pnas.1814279116 Medline

34. R. Evans, M. O'Neill, A. Pritzel, N. Antropova, A. Senior, T. Green, A. Žídek, R. Bates, S. Blackwell, J. Yim, O. Ronneberger, S. Bodenstein, M. Zielinski, A. Bridgland, A. Potapenko, A. Cowie, K. Tunyasuvunakool, R. Jain, E. Clancy, P. Kohli, J. Jumper, D.

Hassabis, Protein complex prediction with AlphaFold-Multimer. bioRxiv 2021.10.04.463034 [Preprint] (2022). https://doi.org/10.1101/2021.10.04.463034

35. R. Diskin, D. Engelberg, O. Livnah, A novel lipid binding site formed by the MAP kinase insert in p38 alpha. *J. Mol. Biol.* **375**, 70–79 (2008). doi:10.1016/j.jmb.2007.09.002 Medline

36. N. Tzarum, Y. Eisenberg-Domovich, J. J. Gills, P. A. Dennis, O. Livnah, Lipid molecules induce p38α activation via a novel molecular switch. *J. Mol. Biol.* **424**, 339–353 (2012). doi:10.1016/j.jmb.2012.10.007 Medline

37. M. Bührmann, J. Hardick, J. Weisner, L. Quambusch, D. Rauh, Covalent Lipid Pocket Ligands Targeting p38α MAPK Mutants. *Angew. Chem. Int. Ed.* **56**, 13232–13236 (2017). doi:10.1002/anie.201706345 Medline

38. M. Bührmann, B. M. Wiedemann, M. P. Müller, J. Hardick, M. Ecke, D. Rauh, Structure-based design, synthesis and crystallization of 2-arylquinazolines as lipid pocket ligands of p38α MAPK. *PLOS ONE* **12**, e0184627 (2017). doi:10.1371/journal.pone.0184627 Medline

39. K. M. Comess, C. Sun, C. Abad-Zapatero, E. R. Goedken, R. J. Gum, D. W. Borhani, M. Argiriadi, D. R. Groebe, Y. Jia, J. E. Clampit, D. L. Haasch, H. T. Smith, S. Wang, D. Song, M. L. Coen, T. E. Cloutier, H. Tang, X. Cheng, C. Quinn, B. Liu, Z. Xin, G. Liu, E. H. Fry, V. Stoll, T. I. Ng, D. Banach, D. Marcotte, D. J. Burns, D. J. Calderwood, P. J. Hajduk, Discovery and characterization of non-ATP site inhibitors of the mitogen activated protein (MAP) kinases. *ACS Chem. Biol.* **6**, 234–244 (2011). doi:10.1021/cb1002619 Medline

40. O. Laufkötter, H. Hu, F. Miljković, J. Bajorath, Structure- and Similarity-Based Survey of Allosteric Kinase Inhibitors, Activators, and Closely Related Compounds. *J. Med. Chem.* **65**, 922–934 (2022). doi:10.1021/acs.jmedchem.0c02076 Medline

41. X. H. Zhang, C.-H. Chen, H. Li, J. Hsiang, X. Wu, W. Hu, D. Horne, S. Nam, J. Shively, S. T. Rosen, Targeting the non-ATP-binding pocket of the MAP kinase p38γ mediates a novel mechanism of cytotoxicity in cutaneous T-cell lymphoma (CTCL). *FEBS Lett.* **595**, 2570–2592 (2021). doi:10.1002/1873-3468.14186 Medline

42. K. Kirsch, A. Zeke, O. Tőke, P. Sok, A. Sethi, A. Sebő, G. S. Kumar, P. Egri, Á. L. Póti, P. Gooley, W. Peti, I. Bento, A. Alexa, A. Reményi, Co-regulation of the transcription controlling ATF2 phosphoswitch by JNK and p38. *Nat. Commun.* **11**, 5769 (2020). doi:10.1038/s41467-020-19582-3 Medline

43. X. Liu, C.-S. Zhang, C. Lu, S.-C. Lin, J.-W. Wu, Z.-X. Wang, A conserved motif in JNK/p38-specific MAPK phosphatases as a determinant for JNK1 recognition and inactivation. *Nat. Commun.* **7**, 10879 (2016). doi:10.1038/ncomms10879 Medline

44. E. I. James, T. A. Murphree, C. Vorauer, J. R. Engen, M. Guttman, Advances in Hydrogen/Deuterium Exchange Mass Spectrometry and the Pursuit of Challenging Biological Systems. *Chem. Rev.* **122**, 7562–7623 (2022). doi:10.1021/acs.chemrev.1c00279 Medline

45. S. A. Foster, D. M. Whalen, A. Özen, M. J. Wongchenko, J. Yin, I. Yen, G. Schaefer, J. D. Mayfield, J. Chmielecki, P. J. Stephens, L. A. Albacker, Y. Yan, K. Song, G. Hatzivassiliou, C. Eigenbrot, C. Yu, A. S. Shaw, G. Manning, N. J. Skelton, S. G.

Hymowitz, S. Malek, Activation Mechanism of Oncogenic Deletion Mutations in BRAF, EGFR, and HER2. *Cancer Cell* **29**, 477–493 (2016). doi:10.1016/j.ccell.2016.02.010 Medline

46. B. Zhang, Y. Chen, P. Dai, H. Yu, J. Ma, C. Chen, Y. Zhang, Y. Guan, R. Chen, T. Liu, J. Wang, L. Yang, X. Yi, X. Xia, H. Ma, Oncogenic mutations within the β3-αC loop of EGFR/ERBB2/BRAF/MAP2K1 predict response to therapies. *Mol. Genet. Genomic Med.* **8**, e1395 (2020). doi:10.1002/mgg3.1395 Medline

47. A. Pérez-Gallegos, M. Garcia-Viloca, À. González-Lafont, J. M. Lluch, A QM/MM study of Kemptide phosphorylation catalyzed by protein kinase A. The role of Asp166 as a general acid/base catalyst. *Phys. Chem. Chem. Phys.* **17**, 3497–3511 (2015). doi:10.1039/C4CP03579H Medline

48. A. Kuzmanic, L. Sutto, G. Saladino, A. R. Nebreda, F. L. Gervasio, M. Orozco, Changes in the free-energy landscape of p38α MAP kinase through its canonical activation and binding events as studied by enhanced molecular dynamics simulations. *eLife* **6**, e22175 (2017). doi:10.7554/eLife.22175 Medline

49. S. Doerr, G. De Fabritiis, On-the-Fly Learning and Sampling of Ligand Binding by High-Throughput Molecular Simulations. *J. Chem. Theory Comput.* **10**, 2064–2069 (2014). doi:10.1021/ct400919u Medline

50. N. Plattner, S. Doerr, G. De Fabritiis, F. Noé, Complete protein-protein association kinetics in atomic detail revealed by molecular dynamics simulations and Markov modelling. *Nat. Chem.* **9**, 1005–1011 (2017). doi:10.1038/nchem.2785 Medline

51. F. Pesce, K. Lindorff-Larsen, Refining conformational ensembles of flexible proteins against small-angle x-ray scattering data. *Biophys. J.* **120**, 5124–5135 (2021). doi:10.1016/j.bpj.2021.10.003 Medline

52. A. H. Larsen, Y. Wang, S. Bottaro, S. Grudinin, L. Arleth, K. Lindorff-Larsen, Combining molecular dynamics simulations with small-angle X-ray and neutron scattering data to study multi-domain proteins in solution. *PLOS Comput. Biol.* **16**, e1007870 (2020). doi:10.1371/journal.pcbi.1007870 Medline

53. S. Orioli, A. H. Larsen, S. Bottaro, K. Lindorff-Larsen, How to learn from inconsistencies: Integrating molecular simulations with experimental data. *Prog. Mol. Biol. Transl. Sci.* **170**, 123–176 (2020). doi:10.1016/bs.pmbts.2019.12.006 Medline

54. N. S. González-Foutel, J. Glavina, W. M. Borcherds, M. Safranchik, S. Barrera-Vilarmau, A. Sagar, A. Estaña, A. Barozet, N. A. Garrone, G. Fernandez-Ballester, C. Blanes-Mira, I. E. Sánchez, G. de Prat-Gay, J. Cortés, P. Bernadó, R. V. Pappu, A. S. Holehouse, G. W. Daughdrill, L. B. Chemes, Conformational buffering underlies functional selection in intrinsically disordered protein regions. *Nat. Struct. Mol. Biol.* **29**, 781–790 (2022). doi:10.1038/s41594-022-00811-w Medline

55. Y. Fleming, C. G. Armstrong, N. Morrice, A. Paterson, M. Goedert, P. Cohen, Synergistic activation of stress-activated protein kinase 1/c-Jun N-terminal kinase (SAPK1/JNK) isoforms by mitogen-activated protein kinase kinase 4 (MKK4) and MKK7. *Biochem. J.* **352**, 145–154 (2000). doi:10.1042/bj3520145 Medline

56. C. Tournier, A. J. Whitmarsh, J. Cavanagh, T. Barrett, R. J. Davis, The MKK7 gene encodes a group of c-Jun NH2-terminal kinase kinases. *Mol. Cell. Biol.* **19**, 1569–1581 (1999). doi:10.1128/MCB.19.2.1569 Medline

57. T. O. Fischmann, C. K. Smith, T. W. Mayhood, J. E. Myers Jr., P. Reichert, A. Mannarino, D. Carr, H. Zhu, J. Wong, R.-S. Yang, H. V. Le, V. S. Madison, Crystal structures of MEK1 binary and ternary complexes with nucleotides and inhibitors. *Biochemistry* **48**, 2661–2674 (2009). doi:10.1021/bi801898e Medline

58. V. Modi, R. L. Dunbrack Jr., A Structurally-Validated Multiple Sequence Alignment of 497 Human Protein Kinase Domains. *Sci. Rep.* **9**, 19790 (2019). doi:10.1038/s41598-019-56499-4 Medline

59. Y. Y. Zhang, J. W. Wu, Z. X. Wang, A distinct interaction mode revealed by the crystal structure of the kinase p38α with the MAPK binding domain of the phosphatase MKP5. *Sci. Signal.* **4**, ra88 (2011). doi:10.1126/scisignal.2002241 Medline

60. C. Dominguez, D. A. Powers, N. Tamayo, p38 MAP kinase inhibitors: Many are made, but few are chosen. *Curr. Opin. Drug Discov. Devel.* **8**, 421–430 (2005). Medline

61. Y. L. Wang, Y.-Y. Zhang, C. Lu, W. Zhang, H. Deng, J.-W. Wu, J. Wang, Z.-X. Wang, Kinetic and mechanistic studies of p38α MAP kinase phosphorylation by MKK6. *FEBS J.* **286**, 1030–1052 (2019). doi:10.1111/febs.14762 Medline

62. J. M. Humphreys, A. T. Piala, R. Akella, H. He, E. J. Goldsmith, Precisely ordered phosphorylation reactions in the p38 mitogen-activated protein (MAP) kinase cascade. *J. Biol. Chem.* **288**, 23322–23330 (2013). doi:10.1074/jbc.M113.462101 Medline

63. K. Aoki, K. Takahashi, K. Kaizu, M. Matsuda, A quantitative model of ERK MAP kinase phosphorylation in crowded media. *Sci. Rep.* **3**, 1541 (2013). doi:10.1038/srep01541 Medline

64. C. Salazar, T. Höfer, Multisite protein phosphorylation—From molecular mechanisms to kinetic models. *FEBS J.* **276**, 3177–3198 (2009). doi:10.1111/j.1742-4658.2009.07027.x Medline

65. A. Punjani, J. L. Rubinstein, D. J. Fleet, M. A. Brubaker, cryoSPARC: Algorithms for rapid unsupervised cryo-EM structure determination. *Nat. Methods* **14**, 290–296 (2017). doi:10.1038/nmeth.4169 Medline

66. F. L. Gervasio, I. Galdadas, D. Gobbo, Architecture of the MKK6-p38α complex defines the basis of MAPK specificity and activation, Yareta (2023); https://doi.org/10.26037/yareta:jmnbt6lzkrfrpdcf3m3343smxq.

67. S. K. Albanese, D. L. Parton, M. Işık, L. Rodríguez-Laureano, S. M. Hanson, J. M. Behr, S. Gradia, C. Jeans, N. M. Levinson, M. A. Seeliger, J. D. Chodera, An Open Library of Human Kinase Domain Constructs for Automated Bacterial Expression. *Biochemistry* **57**, 4675–4689 (2018). doi:10.1021/acs.biochem.7b01081 Medline

68. Y. Nie, I. Bellon-Echeverria, S. Trowitzsch, C. Bieniossek, I. Berger, Multiprotein complex production in insect cells by using polyproteins. *Methods Mol. Biol.* **1091**, 131–141 (2014). doi:10.1007/978-1-62703-691-7_8 Medline

69. M. D. Tully, N. Tarbouriech, R. P. Rambo, S. Hutin, Analysis of SEC-SAXS data via EFA deconvolution and Scatter. *J. Vis. Exp.* (167): (2021). doi:10.3791/61578 Medline

70. D. Schneidman-Duhovny, M. Hammel, J. A. Tainer, A. Sali, Accurate SAXS profile computation and its assessment by contrast variation experiments. *Biophys. J.* **105**, 962–974 (2013). doi:10.1016/j.bpj.2013.07.020 Medline

71. F. Weis, W. J. H. Hagen, Combining high throughput and high quality for cryo-electron microscopy data collection. *Acta Crystallogr. D* **76**, 724–728 (2020). doi:10.1107/S2059798320008347 Medline

72. M. Schorb, I. Haberbosch, W. J. H. Hagen, Y. Schwab, D. N. Mastronarde, Software tools for automated transmission electron microscopy. *Nat. Methods* **16**, 471–477 (2019). doi:10.1038/s41592-019-0396-9 Medline

73. A. J. Jakobi, M. Wilmanns, C. Sachse, Model-based local density sharpening of cryo-EM maps. *eLife* **6**, e27131 (2017). doi:10.7554/eLife.27131 Medline

74. A. Waterhouse, M. Bertoni, S. Bienert, G. Studer, G. Tauriello, R. Gumienny, F. T. Heer, T. A. P. de Beer, C. Rempfer, L. Bordoli, R. Lepore, T. Schwede, SWISS-MODEL: Homology modelling of protein structures and complexes. *Nucleic Acids Res.* **46** (W1), W296–W303 (2018). doi:10.1093/nar/gky427 Medline

75. P. V. Afonine, B. K. Poon, R. J. Read, O. V. Sobolev, T. C. Terwilliger, A. Urzhumtsev, P. D. Adams, Real-space refinement in PHENIX for cryo-EM and crystallography. *Acta Crystallogr. D* **74**, 531–544 (2018). doi:10.1107/S2059798318006551 Medline

76. P. Emsley, K. Cowtan, Coot: Model-building tools for molecular graphics. *Acta Crystallogr. D* **60**, 2126–2132 (2004). doi:10.1107/S0907444904019158 Medline

77. E. F. Pettersen, T. D. Goddard, C. C. Huang, E. C. Meng, G. S. Couch, T. I. Croll, J. H. Morris, T. E. Ferrin, UCSF ChimeraX: Structure visualization for researchers, educators, and developers. *Protein Sci.* **30**, 70–82 (2021). doi:10.1002/pro.3943 Medline

78. E. Pellegrini, D. Piano, M. W. Bowler, Direct cryocooling of naked crystals: Are cryoprotection agents always necessary? *Acta Crystallogr. D* **67**, 902–906 (2011). doi:10.1107/S0907444911031210 Medline

79. M. W. Bowler, M. Guijarro, S. Petitdemange, I. Baker, O. Svensson, M. Burghammer, C. Mueller-Dieckmann, E. J. Gordon, D. Flot, S. M. McSweeney, G. A. Leonard, Diffraction cartography: Applying microbeams to macromolecular crystallography sample evaluation and data collection. *Acta Crystallogr. D* **66**, 855–864 (2010). doi:10.1107/S0907444910019591 Medline

80. O. Svensson, S. Malbet-Monaco, A. Popov, D. Nurizzo, M. W. Bowler, Fully automatic characterization and data collection from crystals of biological macromolecules. *Acta Crystallogr. D* **71**, 1757–1767 (2015). doi:10.1107/S1399004715011918 Medline

81. W. Kabsch, XDS. *Acta Crystallogr. D* **66**, 125–132 (2010). doi:10.1107/S0907444909047337 Medline

82. M. D. Winn, C. C. Ballard, K. D. Cowtan, E. J. Dodson, P. Emsley, P. R. Evans, R. M. Keegan, E. B. Krissinel, A. G. W. Leslie, A. McCoy, S. J. McNicholas, G. N. Murshudov, N. S. Pannu, E. A. Potterton, H. R. Powell, R. J. Read, A. Vagin, K. S. Wilson, Overview of the CCP4 suite and current developments. *Acta Crystallogr. D* **67**, 235–242 (2011). doi:10.1107/S0907444910045749 Medline

83. A. Vagin, A. Teplyakov, Molecular replacement with MOLREP. *Acta Crystallogr. D* **66**, 22–25 (2010). doi:10.1107/S0907444909042589 Medline

84. P. V. Afonine, R. W. Grosse-Kunstleve, N. Echols, J. J. Headd, N. W. Moriarty, M. Mustyakimov, T. C. Terwilliger, A. Urzhumtsev, P. H. Zwart, P. D. Adams, Towards automated crystallographic structure refinement with phenix.refine. *Acta Crystallogr. D* **68**, 352–367 (2012). doi:10.1107/S0907444912001308 Medline

85. V. B. Chen, W. B. Arendall 3rd, J. J. Headd, D. A. Keedy, R. M. Immormino, G. J. Kapral, L. W. Murray, J. S. Richardson, D. C. Richardson, MolProbity: All-atom structure validation for macromolecular crystallography. *Acta Crystallogr. D* **66**, 12–21 (2010). doi:10.1107/S0907444909042073 Medline

86. M. Mirdita, K. Schütze, Y. Moriwaki, L. Heo, S. Ovchinnikov, M. Steinegger, ColabFold: Making protein folding accessible to all. *Nat. Methods* **19**, 679–682 (2022). doi:10.1038/s41592-022-01488-1 Medline

87. H. Wang, W.-T. Lo, A. Vujičić Žagar, F. Gulluni, M. Lehmann, L. Scapozza, V. Haucke, O. Vadas, Autoregulation of Class II Alpha PI3K Activity by Its Lipid-Binding PX-C2 Domain Module. *Mol. Cell* **71**, 343–351.e4 (2018). doi:10.1016/j.molcel.2018.06.042 Medline

88. Y. Perez-Riverol, J. Bai, C. Bandla, D. García-Seisdedos, S. Hewapathirana, S. Kamatchinathan, D. J. Kundu, A. Prakash, A. Frericks-Zipper, M. Eisenacher, M. Walzer, S. Wang, A. Brazma, J. A. Vizcaíno, The PRIDE database resources in 2022: A hub for mass spectrometry-based proteomics evidences. *Nucleic Acids Res.* **50** (D1), D543–D552 (2022). doi:10.1093/nar/gkab1038 Medline

89. C. S. Hughes, S. Foehr, D. A. Garfield, E. E. Furlong, L. M. Steinmetz, J. Krijgsveld, Ultrasensitive proteome analysis using paramagnetic bead technology. *Mol. Syst. Biol.* **10**, 757 (2014). doi:10.15252/msb.20145625 Medline

90. H. Franken, T. Mathieson, D. Childs, G. M. A. Sweetman, T. Werner, I. Tögel, C. Doce, S. Gade, M. Bantscheff, G. Drewes, F. B. M. Reinhard, W. Huber, M. M. Savitski, Thermal proteome profiling for unbiased identification of direct and indirect drug targets using multiplexed quantitative mass spectrometry. *Nat. Protoc.* **10**, 1567–1593 (2015). doi:10.1038/nprot.2015.101 Medline

91. R. A. Friesner, R. B. Murphy, M. P. Repasky, L. L. Frye, J. R. Greenwood, T. A. Halgren, P. C. Sanschagrin, D. T. Mainz, Extra precision glide: Docking and scoring incorporating a model of hydrophobic enclosure for protein-ligand complexes. *J. Med. Chem.* **49**, 6177–6196 (2006). doi:10.1021/jm051256o Medline

92. A. Šali, T. L. Blundell, Comparative protein modelling by satisfaction of spatial restraints. *J. Mol. Biol.* **234**, 779–815 (1993). doi:10.1006/jmbi.1993.1626 Medline

93. G. Martínez-Rosell, T. Giorgino, G. De Fabritiis, PlayMolecule ProteinPrepare: A Web Application for Protein Preparation for Molecular Dynamics Simulations. *J. Chem. Inf. Model.* **57**, 1511–1516 (2017). doi:10.1021/acs.jcim.7b00190 Medline

94. K. L. Meagher, L. T. Redman, H. A. Carlson, Development of polyphosphate parameters for use with the AMBER force field. *J. Comput. Chem.* **24**, 1016–1025 (2003). doi:10.1002/jcc.10262 Medline

95. F. P. Buelens, H. Leonov, B. L. de Groot, H. Grubmüller, ATP-Magnesium Coordination: Protein Structure-Based Force Field Evaluation and Corrections. *J. Chem. Theory Comput.* **17**, 1922–1930 (2021). doi:10.1021/acs.jctc.0c01205 Medline

96. M. J. Abraham, T. Murtola, R. Schulz, S. Páll, J. C. Smith, B. Hess, E. Lindahl, GROMACS: High performance molecular simulations through multi-level parallelism from laptops to supercomputers. *SoftwareX* **1-2**, 19–25 (2015). doi:10.1016/j.softx.2015.06.001

97. G. A. Tribello, M. Bonomi, D. Branduardi, C. Camilloni, G. Bussi, PLUMED 2: New feathers for an old bird. *Comput. Phys. Commun.* **185**, 604–613 (2014). doi:10.1016/j.cpc.2013.09.018

98. G. Bussi, D. Donadio, M. Parrinello, Canonical sampling through velocity rescaling. *J. Chem. Phys.* **126**, 014101 (2007). doi:10.1063/1.2408420 Medline

99. M. Bernetti, G. Bussi, Pressure control using stochastic cell rescaling. *J. Chem. Phys.* **153**, 114107 (2020). doi:10.1063/5.0020514 Medline

100. M. Marchi, P. Ballone, Adiabatic bias molecular dynamics: A method to navigate the conformational space of complex molecular systems. *J. Chem. Phys.* **110**, 3697–3702 (1999). doi:10.1063/1.478259

101. S. Doerr, M. J. Harvey, F. Noé, G. De Fabritiis, HTMD: High-Throughput Molecular Dynamics for Molecular Discovery. *J. Chem. Theory Comput.* **12**, 1845–1852 (2016). doi:10.1021/acs.jctc.6b00049 Medline

102. G. Pérez-Hernández, F. Paul, T. Giorgino, G. De Fabritiis, F. Noé, Identification of slow molecular order parameters for Markov model construction. *J. Chem. Phys.* **139**, 015102 (2013). doi:10.1063/1.4811489 Medline

103. P. Raiteri, A. Laio, F. L. Gervasio, C. Micheletti, M. Parrinello, Efficient reconstruction of complex free energy landscapes by multiple walkers metadynamics. *J. Phys. Chem. B* **110**, 3533–3539 (2006). doi:10.1021/jp054359r Medline

104. X. Daura, K. Gademann, B. Jaun, D. Seebach, W. F. van Gunsteren, A. E. Mark, Peptide Folding: When Simulation Meets Experiment. *Angew. Chem. Int. Ed.* **38**, 236–240 (1999). doi:10.1002/(SICI)1521-3773(19990115)38:1/2<236::AID-ANIE236>3.0.CO;2-M

105. S. Röblitz, M. Weber, Fuzzy spectral clustering by PCCA+: Application to Markov state models and data classification. *Adv. Data Anal. Classif.* **7**, 147–179 (2013). doi:10.1007/s11634-013-0134-6

106. S. Bottaro, G. Bussi, S. D. Kennedy, D. H. Turner, K. Lindorff-Larsen, Conformational ensembles of RNA oligonucleotides from integrating NMR and molecular simulations. *Sci. Adv.* **4**, eaar8521 (2018). doi:10.1126/sciadv.aar8521 Medline

107. S. Grudinin, M. Garkavenko, A. Kazennov, Pepsi-SAXS: An adaptive method for rapid and accurate computation of small-angle X-ray scattering profiles. *Acta Crystallogr. D* **73**, 449–464 (2017). doi:10.1107/S2059798317005745 Medline

108. S. Bottaro, T. Bengtsen, K. Lindorff-Larsen, in *Structural Bioinformatics: Methods and Protocols,* Z. Gáspári, Ed. (Springer, 2020), pp. 219–240.

109. F. Pesce, K. Lindorff-Larsen, Combining Experiments and Simulations to Examine the Temperature-Dependent Behavior of a Disordered Protein. *J. Phys. Chem. B* **127**, 6277–6286 (2023). doi:10.1021/acs.jpcb.3c01862 Medline

110. I. Galdadas, L. Carlino, R. A. Ward, S. J. Hughes, S. Haider, F. L. Gervasio, Structural basis of the effect of activating mutations on the EGF receptor. *eLife* **10**, e65824 (2021). doi:10.7554/eLife.65824 Medline

111. Y. Shan, A. Arkhipov, E. T. Kim, A. C. Pan, D. E. Shaw, Transitions to catalytically inactive conformations in EGFR kinase. *Proc. Natl. Acad. Sci. U.S.A.* **110**, 7270–7275 (2013). doi:10.1073/pnas.1220843110 Medline

112. J. Eswaran, A. Bernad, J. M. Ligos, B. Guinea, J. É. Debreczeni, F. Sobott, S. A. Parker, R. Najmanovich, B. E. Turk, S. Knapp, Structure of the human protein kinase MPSK1 reveals an atypical activation loop architecture. *Structure* **16**, 115–124 (2008). doi:10.1016/j.str.2007.10.026 Medline